Title

The spatial periodic computation of hippocampus-entorhinal circuit in navigation

Author list

Bo Zhang[1,2], and Jia Liu[2]*

Affiliations

[1] Beijing Academy of Artificial Intelligence, Beijing, 100084, China

[2] Tsinghua Laboratory of Brain and Intelligence & Department of Psychological and Cognitive Sciences, Tsinghua University, Beijing, 100084, China

*Correspondence shall be addressed to: JL, liujiathu@tsinghua.edu.cn

Summary

To achieve the computational goal of navigating in both physical and mental spaces, human brain employs a cognitive map constructed by the global metrics of the entorhinal cortex and the local locations of the hippocampus. However, how these two regions work collaboratively in navigation remains unclear. Here, we designed an object-matching task where human participants unknowingly manipulated object variants arranged in a ring-like structure around a central prototype. Functional MRI revealed a 3-fold spatial periodicity of hippocampal activity, which tracked the navigation path from the original object variants to the central prototype in the object space. Importantly, this spatial periodicity of the hippocampus was phase-locked with the well-documented 6-fold periodicity of the entorhinal cortex, suggesting a periodic scaffold connecting these two regions. In addition, a 3-fold periodicity was found embedded in human behavior, which fluctuated as a function of the navigation path and phase-locked with hippocampal activity. Finally, we proposed an E-H PhaseSync model to illustrate that the spatial periodicity originated from the population activity of entorhinal grid cells may serve as a scaffold in the hippocampal-entorhinal network, where hippocampal vector fields emerge as the neural basis for utilizing the cognitive map in navigation.

Keywords

Entorhinal grid cells, Hippocampal place cells, Cognitive map, Spatial periodicity, fMRI

Introduction

The cognitive map, introduced by Tolman (1) and elaborated through the discovery of hippocampal place cells (2), represents a mental framework of spatial and conceptual relationships (3-5) to facilitate knowledge retrieval and decision-making (6-10). However, how the abstract relationships encoded by the hippocampus (HPC) are actualized in navigating both spatial and conceptual spaces remain somewhat unclear. A recent study by Ormond and O'Keefe (11) sheds light on this issue by unveiling the convergence sinks (ConSinks) of place cells in the HPC, where these ConSinks, characterized by vector fields, were distributed throughout the environment and provided gradient signals to guide navigation from self-location towards the intended goal-location. This finding may underscore vector-based computation of the HPC in constructing conceptual "spatial path" during navigation. In the present study, we further asked how hippocampal vector fields, which represent the path from self-location and the goal-location, are constructed during navigation.

Anatomically, the entorhinal cortex (ERC) serves as one of the major projections to its downstream HPC (12-14), and complete lesions of the ERC substantially disrupt the precision and stability of the spatial representations of the HPC (15). Entorhinal grid cells, known for their hexagonal firing pattern as a spatial metric of space (16), are proposed by several computational models as the foundation for place field formation through phase vectors of multi-scale grid modules and the winner-take-all dynamics (17-21). In addition, empirical evidence demonstrates the role of grid cells in tracking location, direction, and velocity, essential for navigation (22-24). Those results collectively support the possibility that grid cells may serve as the geometric framework with periodic codes to promote the formation of hippocampal vector fields of place cells via the ERC-HPC circuitry. If this conjecture is valid, we might expect to find spatial periodicity in the HPC, which would likely be a manifestation of hippocampal vector fields of place cells at the population level, based on the observation of the nearly invariant orientation and spacing of grid cells at populational level (16, 22, 25, 26).

The examination of this idea requires simultaneously recording ERC and HPC activity at the populational level, putting great challenges on electrophysiological and two-

photon calcium imaging on animals' brains. Functional MRI (fMRI), which offers a broader scope, have been employed to explore the spatial periodicity of entorhinal grid cells at the population level and successfully identify a 6-fold periodicity as a function of movement directions when navigating in both spatial and conceptual spaces (27-31). Consequently, in this study we used fMRI with human participants to explore whether there is spatial periodicity in the HPC and, critically, whether this spatial periodicity, if observed, is phase-locked with that of the ERC.

To do this, we designed an object matching task where participants were instructed to morph object variants to match the target prototype by navigating in a 2-dimensional greeble space (Fig.1). To explore potential spatial periodicity in the HPC, starting-locations were arranged in a ring-shaped pattern, with each location corresponding to a unique conceptual direction towards the goal ranging from 0° to 360°. Both sinusoid and spectral analyses revealed a spatial periodicity of 3-fold modulation in the HPC in two independent participant groups, whose phase was closely coupled with the hexagonal 6-fold periodicity in the ERC. In addition, this 3-fold periodicity was also observed in participants' behavioral performance. Based on these empirical findings, we proposed an E-H PhaseSync model to elucidate the formation of hippocampal vector fields from the projection of grid cell population.

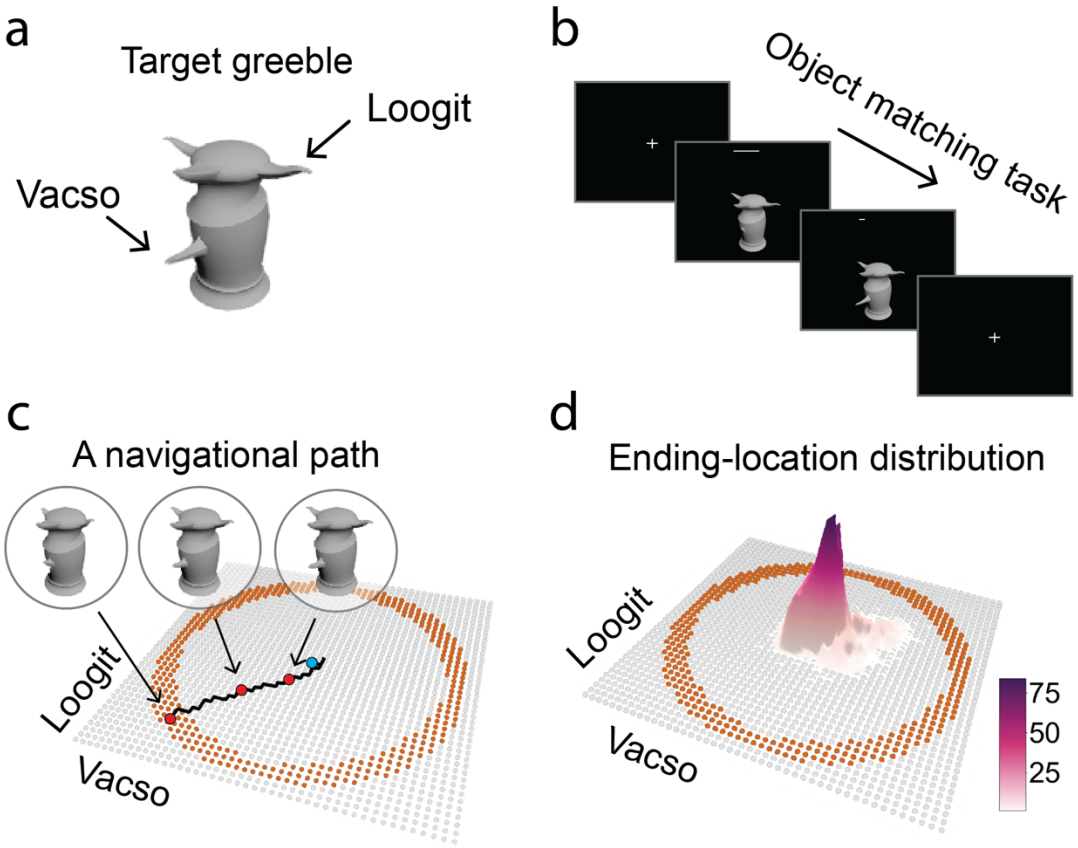

Fig. 1. Experimental design. a) Depiction of the greeble prototype (32) and its two defining features, namely "Loogit" and "Vacso." b) Within the MRI scanner, participants continuously adjusted the length of Loogit and Vacso to match the prototype by button press within a 10-s time limit. c) Conceptual object space. Each orange dot within the ring-shaped area represents a variant greeble, while the central blue dot indicates the prototype greeble (i.e., the goal-location). Red dots denote intermediate locations along the navigational path (i.e., the black line). d) Distribution of the ending-locations, aggregated across participants.

Results

Construction of a conceptual object space

A novel 3D object, named greeble (Fig.1a) (32), was utilized to create a conceptual greeble space. Within this space, locations were represented by a series of unique greeble variants characterized by distinct lengths of their two features, namely "Loogit" and "Vacso,"

which formed the two dimensions of the space. The greeble positioned at the center of the space served as the prototype, acting as the target. In each trial, a greeble variant, pseudo-randomly selected from the periphery of the space, was presented on the screen (Fig.1b). Participants were instructed to adjust the length of Loogit and Vasco independently via button press to match the prototype as accurately as possible. Additionally, they were encouraged to adjust both features simultaneously (i.e., one unit of adjustment on one feature followed by one unit of adjustment on the other). This process generated a navigational path constituted by a sequence of selected greeble variants for each trial (Fig.1c). To ensure comprehensive exploration of the greeble space, greeble variants were evenly sampled, allowing participants experienced conceptual directions ranged from 0° to 360° (i.e., the orange locations in Fig.1c) relative to the goal-location (see Methods for details). Note that no participant was aware of the existence of the greeble space or had a subjective feeling of navigating during the experiment. To examine whether the participants adjusted both features simultaneously (i.e., generating intercardinal directions), rather than adjusting one feature first and then the other (i.e., generating four cardinal directions: North, East, South, and West), we calculated the number of intercardinal directions using every three consecutive steps from their original movements (Fig. S3), and found a significantly higher number of intercardinal directions ($t(19) = 9.353$, $p < 0.001$, two-tailed; Cohen's d = 1.67), confirming that navigational experiences in diverse directions were effectively maintained. Finally, the probability density map of the ending-locations aggregated across trials and across participants showed the peak at the prototype (Fig. 1d), reflecting the successful performance of the task.

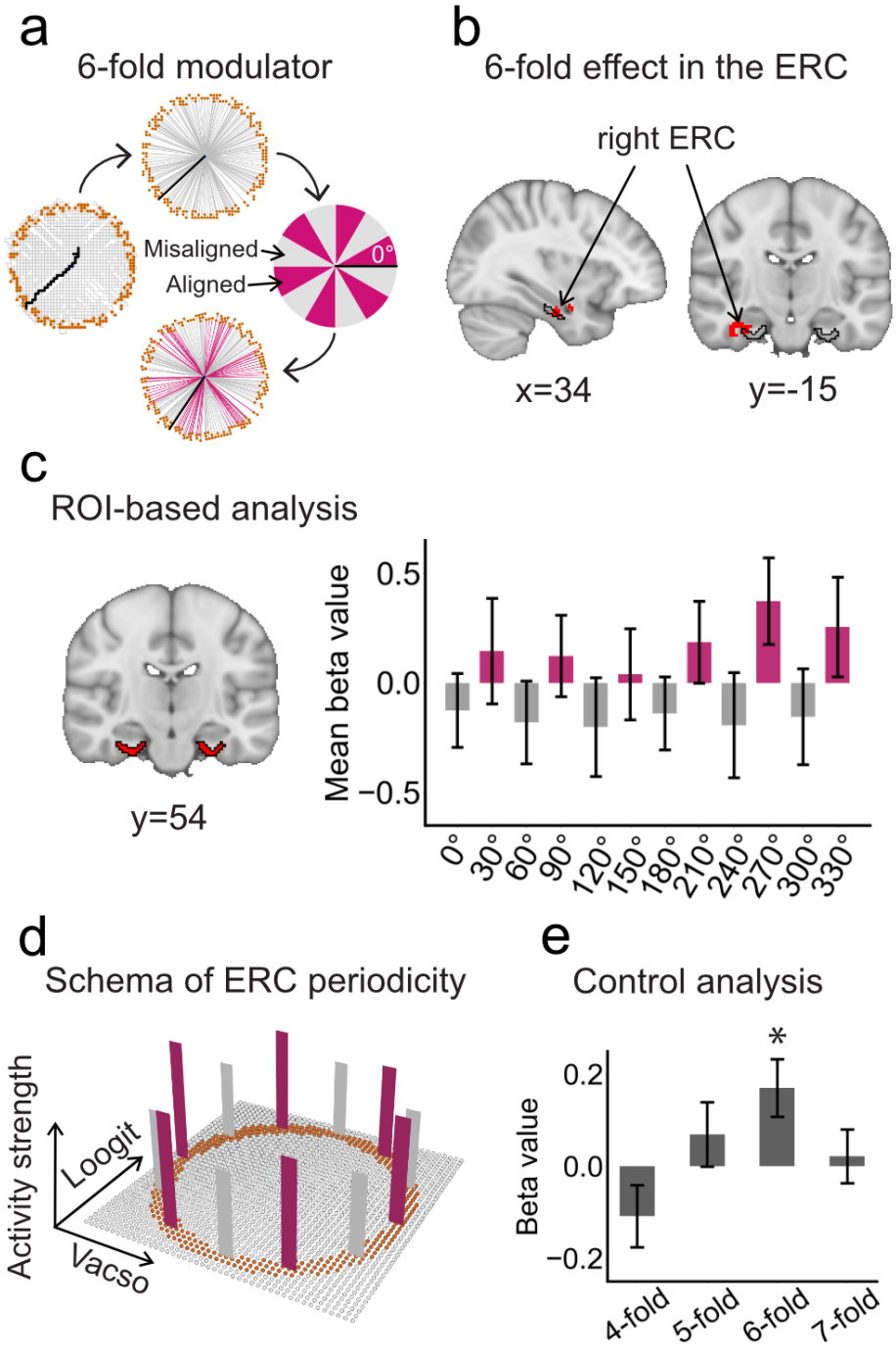

Fig. 2. 6-fold periodicity in the ERC. a) Schematic illustrating the 6-fold modulation for localizing grid cell activity. Participants' paths were simplified from the original path (Left) to straight lines (Top) connecting the starting and the ending-locations. These paths were further categorized into either "aligned" or "misaligned" conditions (Right & Bottom). For each participant's original path, refer to Fig. S2. b) Voxel-based sinusoidal analysis

revealed significant 6-fold periodicity within the right ERC (initial threshold: $p = 0.01$, two-tailed; cluster-based correction for multiple comparisons: $p < 0.05$; Peak MNI coordinate: 32, -16, -28, t(19) = 3.74). The black outline indicates the ERC. c) BOLD activity of bilateral ERC reconstructed from sinusoidal analysis showed significant 6-fold periodicity as a function of movement directions ($p < 0.05$, corrected for multiple comparison). d) Schema illustrating the 6-fold periodicity in the 2D space. e) ROI analysis replicated the 6-fold periodicity of the ERC compared to 4-, 5- and 7-fold periodicity (6-fold: t(19) = 2.66, $p = 0.02$, two tailed; Cohen's d = 0.59; 4-, 5-, 7-fold: $p > 0.05$).

6-fold periodicity in the ERC

In the fMRI analysis reported here, we combined participants from both experimental and replication groups to demonstrate more reliable results with greater statistical power. For similar results from each group, refer to Fig. S7. Using the sinusoidal analysis (27-31), we replicated previous findings that the BOLD signal in the ERC is stronger during movement direction aligned with grid axes (Fig. 2a; i.e., aligned condition) and weaker when misaligned with grid axes (i.e., misaligned condition), characterized by a 60° periodicity. First, grid orientation, determining the grid axes, was computed for each voxel within the bilateral ERC using half of the data (Experimental session 1, 3, 5, 7; see Methods for details). Significant deviations from uniform grid orientations were observed for all participants (Fig.S4, $p < 0.05$; Rayleigh test of uniformity, Bonferroni corrected). Second, hexagonal activity in the other half of the data (Experimental session 2, 4, 6, 8) was examined using participants' movement directions, calibrated by the grid orientation so that all participants had identical phases of 6-fold periodicity (arbitrarily defined 0° shown in Fig.2a) tracking their movement directions. The result identified a significant cluster in the right ERC (Fig.1b; initial threshold: $p = 0.01$, two-tailed; cluster-based correction for multiple comparisons: $p < 0.05$; Peak MNI coordinate: 32, -16, -28, t(19) = 3.74). Next, we examined hexagonal activity using a bilaterally hand-drawn ERC mask (Fig. 2C, left). The BOLD signal reconstructed from sinusoidal analysis revealed significant 6-fold periodicity as a function of movement directions (Fig.2C, right; $p < 0.05$, permutation corrected for multiple comparison), suggesting periodic representation of the conceptual directions in the 2D greeble space by the ERC (Fig. 2d). An additional ROI analysis of

bilateral ERC corroborated the robustness of the 6-fold periodicity (Fig. 2e; $t(19) = 2.6586$, $p = 0.016$, Cohen's $d = 0.59$). In contrast, no significant clusters were detected for either 4-fold (90° periodicity; $t(19) = -1.5669$, $p = 0.133$, Cohen's $d = -0.35$), 5-fold (72° periodicity; $t(19) = 0.96485$, $p = 0.347$, Cohen's $d = 0.21$), and 7-fold (51.4° periodicity; $t(19) = 0.35718$, $p = 0.725$, Cohen's $d = 0.07$) periodicity. These results replicated the hexagonal activity in the ERC when human participants performed conceptual navigation task (see also 27-31), confirming the effectiveness of our object-match task as a navigation task in the greeble space.

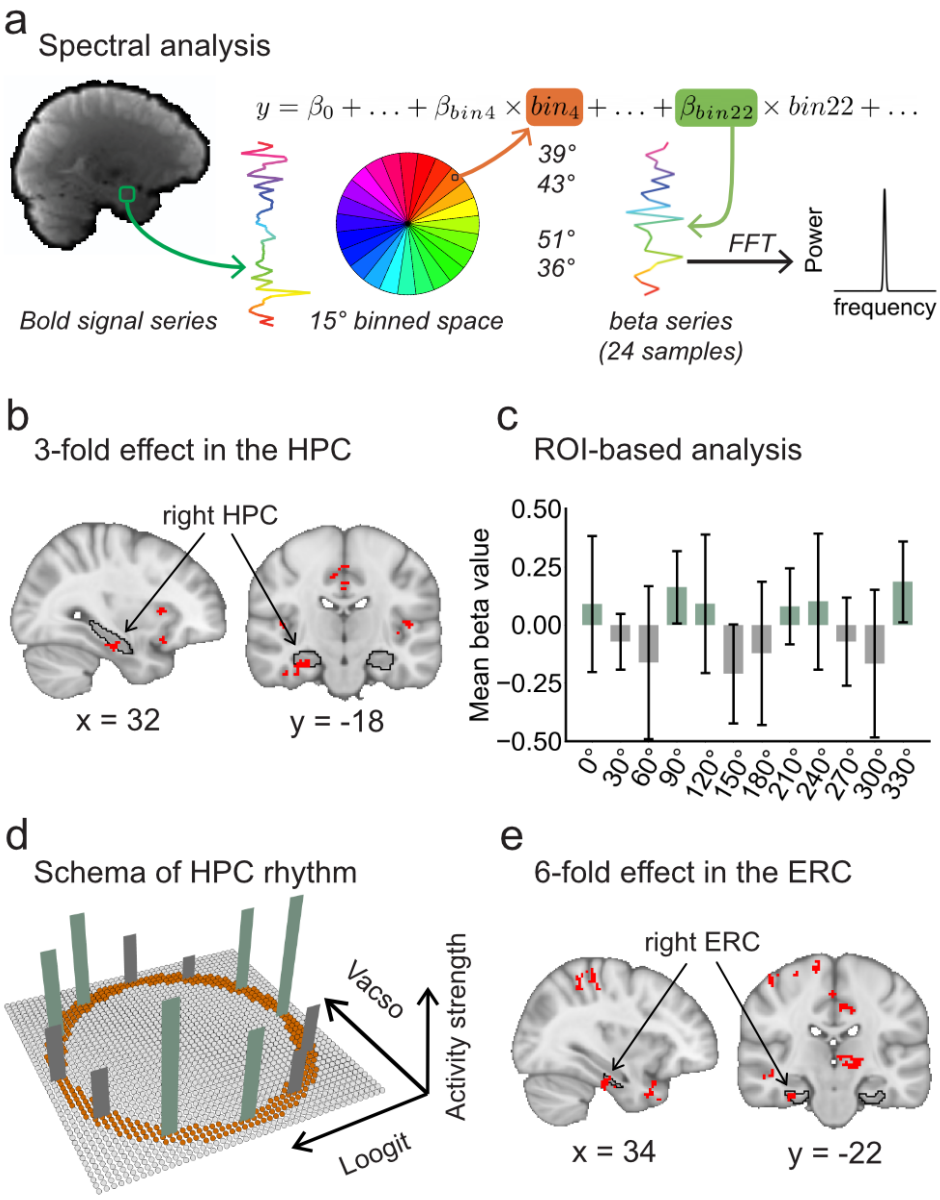

Fig. 3. 3-fold periodicity in the HPC. a) Schema illustrating the procedure of spectral analysis to identify the neural periodicity. b) Voxel-based spectral analysis revealed a significant 3-fold periodicity in the right HPC (initial threshold: p = 0.01, one-tailed; cluster-based correction for multiple comparisons: $p < 0.05$; Peak MNI coordinate: 28, -18, -20, t(19) = 7.06). The black outline indicates the HPC. c) BOLD activity of bilateral HPC reconstructed from sinusoidal analysis showed significant 3-fold periodicity as a function of movement directions (p < 0.05, corrected for multiple comparison). d) Schema

illustrating the 3-fold periodicity in the 2D space, where each path is tracked by a unique phase of HPC activity. e) Voxel-based spectral analysis revealed significant 6-fold periodicity in the right ERC (initial threshold: $p = 0.01$, one-tailed; cluster-based correction for multiple comparisons: $p < 0.05$; Peak MNI coordinate: 34, -24, -24, t(19) = 4.69). The black outline indicates the ERC.

3-fold periodicity in the HPC

Anatomically, HPC receives afferent projections from ERC (12-14), suggesting a potential for observing periodic patterns of the HPC because of the activity periodicity observed in the ERC. To test this intuition, our experimental design mandated that participants explored the full range of conceptual directions, ranged from 0° to 360°, allowing to examine the spatial periodicities of the HPC in addition to the established 60° periodicity in the ERC. Specifically, we employed a spectral analysis to explore periodicity spectrum (Fig.3a). This method does not require prior hypotheses on the phase-offset calibrations as necessitated by sinusoidal analysis (27-31). In this analysis, movement directions of each participant were down-sampled into 15° bins, generating a vector of 24 resampled directions (e.g., 0°, 15°, and 30°), thereby enabling the detection of frequency from 0 Hz to 11 Hz. The direction-dependent brain activities were estimated using a GLM, where each directional bin was specified as a regressor, and were sorted in ascending order. A Fast Discrete Fourier Transform (FFT) was performed on the direction-dependent brain activities (Fig.3a). Spectral power was extracted from each voxel for each of 0 Hz to 11 Hz (see Methods for detail)

A significant cluster of 3-fold periodicity was observed in the right HPC (Fig.3b; initial threshold: P = 0.01, one-tailed; cluster-based correction for multiple comparisons: $p < 0.05$; Peak MNI coordinate: 28, -18, -20, t(19) = 7.06). ROI-based analysis, using an anatomical mask of the bilateral HPC derived from AAL (33), replicated the significant 3-fold periodicity of the HPC activity reconstructed from sinusoidal analysis (Fig.3c; $p < 0.05$, permutation corrected for multiple comparisons), confirming the periodic representation of the HPC in conceptual directions in 2D greeble space, which differed in spatial frequency compared to the ERC (Fig. 2d).

The hippocampal 3-fold periodicity has not been previously reported in the spatial domain either by neurophysiological or fMRI studies. To validate its reliability, we conducted additional analyses. First, the spectral analysis, in addition to revealing the 3-fold periodicity in the HPC, also identified a significant cluster of 6-fold periodicity in the right ERC (Fig.3e; initial threshold: $p = 0.01$, one-tailed; cluster-based correction for multiple comparisons: $p < 0.05$; Peak MNI coordinate: 34, -24, -24, t(19) = 4.69), thereby replicating the finding with the sinusoidal analysis. On the other hand, the sinusoidal analysis also showed a 3-fold periodicity in the right HPC (Fig.S5; initial threshold: $p = 0.05$, two-tailed; cluster-based correction for multiple comparisons: $p < 0.05$; Peak MNI coordinate: 30, -34, -4, t(19) = 3.63). That is, both the spectral and sinusoidal analyses revealed the 3-fold periodicity in the HPC.

Second, the 3-fold periodicity in the HPC was not due to the down-sampling of directions into 15° bins, as consistent findings were observed when 10° and 20° bins were applied (Fig. S6). Third, both HPC and ERC periodicity were reliably detected in both experimental and replication groups (Fig.S7; 3-fold [spectral analysis]: initial threshold: $p = 0.01$, one-tailed. SVC correction of the MTL for multiple comparison: $p < 0.05$; 6-fold [sinusoidal analysis]: initial threshold: $p = 0.01$, two-tailed. SVC correction of the MTL for multiple comparison: $p < 0.05$). Fourth, we examined the whole brain representation of both 3- and 6-fold periodicity, respectively. The 3-fold periodicity was found in the default mode network and the bilateral Heschl's Gyrus (HG) in addition to the HPC. In contrast, 6-fold periodicity was more involved with the visuomotor areas and the bilateral lateral prefrontal cortex (lPFC) in addition to the ERC (Fig.S8; initial threshold: $p = 0.01$, one-tailed; permutation corrected for multiple comparisons: $p < 0.05$), suggesting distinct functional networks involved in processing conceptual directions during navigation. Taken together, these results suggested a robust 3-fold periodicity located in the HPC, which fluctuates as a function of conceptual directions.

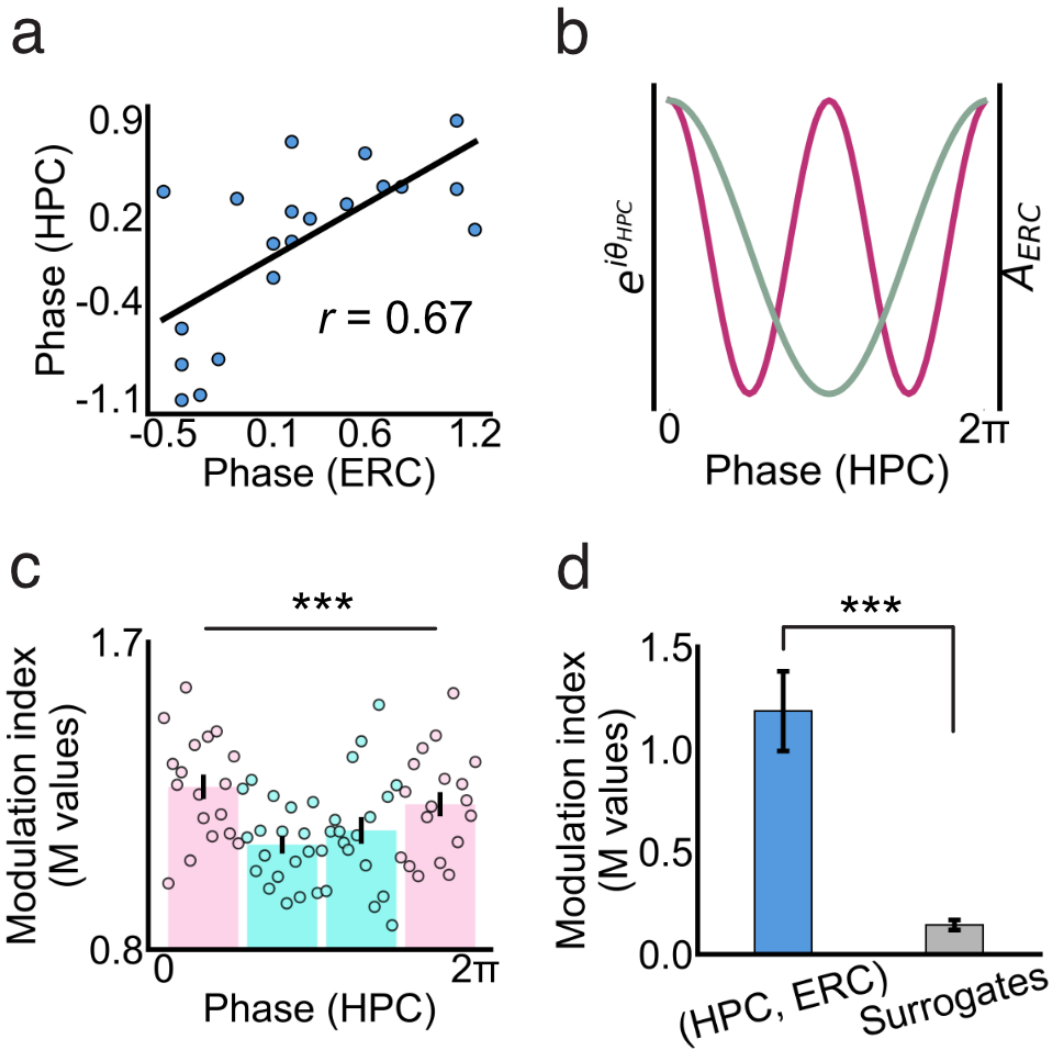

Fig. 4. Phase synchronization of BOLD signals in movement direction between ERC and HPC. a) Cross-participant phase coupling analysis revealed significant correlation between the phase of the ERC and HPC (r = 0.67, p = 0.001), indicating that 3-fold periodicity in the HPC is phase-locked with 6-fold periodicity in the ERC. b) Schema of the peak-overlapped pattern as indicated by the symmetric pattern of modulation index M in corresponding to the phase of the HPC. c) Amplitude-phase modulation analysis showed significantly higher cross-frequency modulation index M in 0° -90° and 270° -360° of the HPC phase compared to 90° -270° (t(68) = 3.45, p < 0.001). d) The modulation index M was significantly higher between the ERC-HPC BOLD signals compared to that of surrogates (t(38) = 5.19, p < 0.001; Cohen's d = 1.09). Error bars indicate SEM. ***: p < 0.001.

To further explore the relationship between the observed periodicity in the HPC and the ERC, we reconstructed the BOLD signal series of the bilateral ERC and HPC using the parameters estimated from sinusoidal analysis for each participant (see Methods for details), and then used cross-participant phase coupling analysis to examine the relation in phase between two periodicities. We found significant ERC-HPC phase coupling (Fig.4a; r = 0.67, p = 0.001) between the 3-fold periodicity in the HPC and the 6-fold periodicity in the ERC, suggesting that the BOLD activities between the HPC and the ERC was phase-locked during navigation.

To quantify the peak offset of the ERC and HPC periodicities, we used cross-frequency amplitude-phase modulation analysis (34). This method measured the composite signal z for each sample of the ERC and HPC activities through $z = A_{ERC}e^{i\phi_{HPC}}$, where A_{ERC} and ϕ_{HPC} represent the amplitude envelope of high-frequency BOLD signals extracted from the ERC and the phase of low-frequency BOLD signals of the HPC, respectively. The modulation index M, defined by the absolute value of the mean of z values, was then calculated for each phase of BOLD signal of the HPC. Therefore, if the periodicities of the HPC and ERC were overlapped at their peaks (i.e., no peak offset), we should expect a symmetric pattern of M in corresponding to the phase of the HPC (Fig.4d). Indeed, this analysis found a U-shaped pattern of the modulation index M (Fig.4b), as shown by the higher M located around the phase 0 and 2pi and lower M located around the phase pi. We separated M from the phase of the HPC (phase 0: 0[0°]-1.57[90°]; phase pi: 1.57[90°]-4.71[270°]; phase 2pi: 4.71[270°]-6.28[360°]). Both phase 0 and phase 2pi showed significantly higher modulations than phase pi (t(68) = 3.45, p < 0.001; Cohen's d = 0.63), while no significant difference in M was found between phase 0 and phase 2pi (t(34) = 0.98, p = 0.33; Cohen's d = 0.21). This U-shaped pattern suggests that there was no peak offset between the BOLD signals of the ERC and HPC, where phase 0 and phase 2pi were associated with the strongest amplitude of the ERC in the cycle of HPC periodicity. To further examine the reliability of this finding, we created a set of surrogates by offsetting the amplitude of the ERC relative to the phase of the HPC by spatial lags, and we found the modulation index of these surrogate controls was significantly lower than that without peak offset (Fig. 4d; t(19) = 5.19, p < 0.001; Cohen's d = 1.09).

Taken together, these results support that the peaks of the ERC selectively aligned with those of the HPC. Note that this result differs from prior work in the temporal domain, where neural coherence is typically characterized by the modulation of low-frequency activity on high-frequency activity (e.g., 35-37). Rather, our results implicate a potential relationship between the 3-fold periodicity of the HPC and 6-fold periodicity of the ERC.

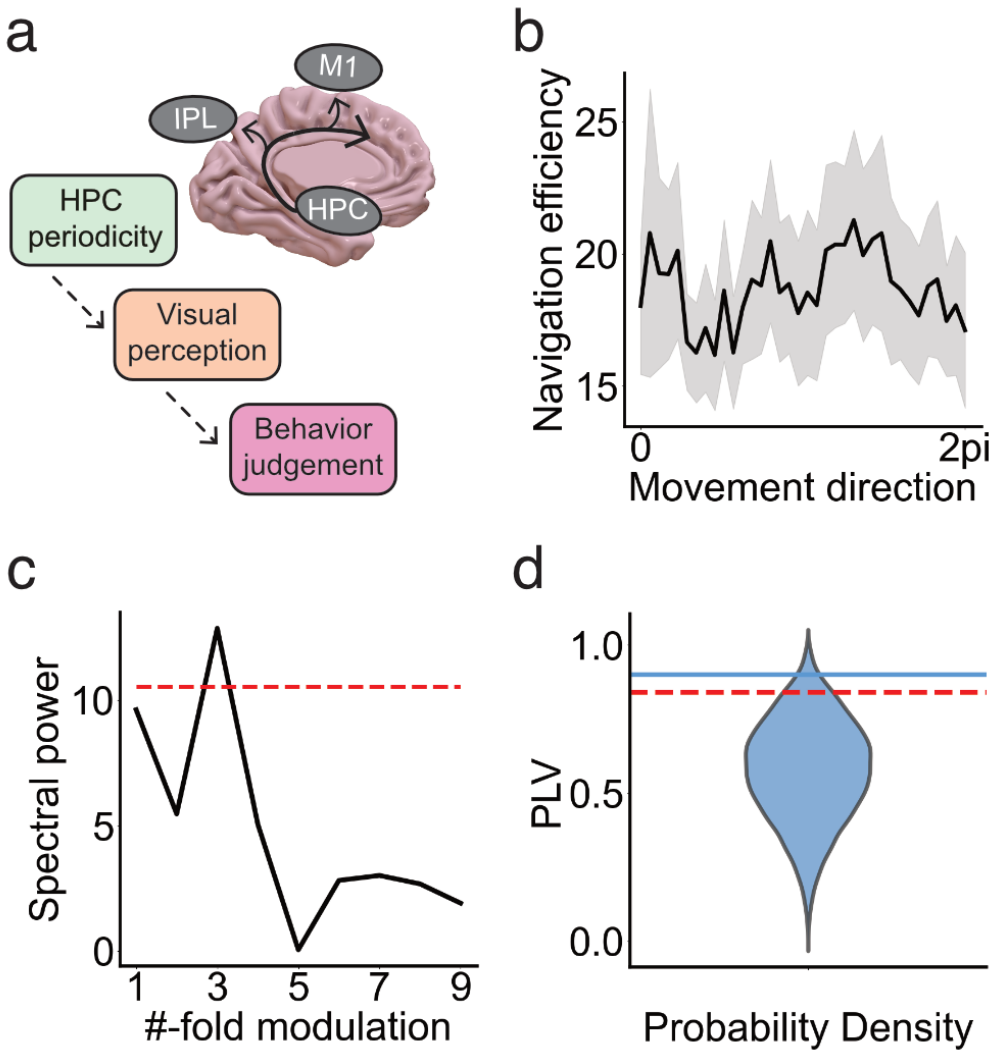

Fig. 5 The 3-fold periodicity in behavioral performance. a) Visuomotor brain circuit potentially inheriting HPC's 3-fold periodicity. IPL: Inferior parietal lobule; M1: Primary Motor Cortex. b) Participants' navigation efficiency, measured by a composite index of path length and deviation from the goal- to ending-locations, fluctuated as a function of movement directions. The shaded area denotes SE. c) The 3-fold periodicity of participants'

performance. Spectral analysis revealed a significant spectral power at the 3-fold periodicity ($p < 0.05$, corrected for multiple comparisons). The red dashed line represents the baseline derived from permutation. d) Behavioral performance phase-locked with the BOLD signals of the HPC. Phase-Locking Value (PLV, blue line) exceeded the threshold (red dashed line) of the 95th percentile of the PLV distribution obtained from randomly shuffled surrogates at 3-fold periodicity ($p < 0.05$, corrected for multiple comparisons).

3-fold periodicity on behavior performance

Considering the anatomy of the visual-motor circuit in the brain, it is plausible that the 3-fold spatial periodicity of the HPC may propagate to egocentric cortical areas such as the inferior parietal lobule (IPL), hereby influencing the visuospatial perception of participants during object matching task (Fig. 5a). To examine this intuition, we evaluated participants' navigational efficiency using two metrics for each trial (Fig.5b; see Methods for details): one was the path length used for completing the trial, and the other was the error size between the actual ending-location and the goal-location, as participants seldom stopped exactly at the goal-location. Better navigation efficiency was indexed by the composite score of shorter travel lengths and smaller error size.

Indeed, we identified a significant behavioral periodicity of the participants with the spectral power peak at 3-fold (Fig. 5c; $p < 0.05$, permutation corrected for multiple comparisons), which could be visually identified from the participant-averaged navigation efficiency fluctuated as a function of movement directions (Fig. 4b). In contrast, no 6-fold behavioral periodicity was found ($p > 0.05$). To further establish the causal relationship between hippocampal and behavioral periodicities, we calculated the phase-locking coherence across participants for each of 0- to 18-fold (i.e., half of the sample size). This analysis revealed significantly higher Phase-Locking Value (PLV) at 3-fold periodicity than the shuffled control (Fig.5d; $p < 0.05$, permutation corrected for multiple comparisons). The 6-fold behavioral periodicity was again not found ($p > 0.05$). Contrary to the commonly held assumption of isotropic performance across movement directions, these results suggested that human behaviors were influenced by the HPC periodicity. Participants tend to perform more efficiently (i.e., shorter path length and smaller error

size) when the movement direction between the starting- and ending-location aligns with the grid axes compared to these of misaligned.

Discussion

Navigation, the process of retrieving spatial relations from one moment to the next in both conceptual (3-6) and physical spaces (1, 2, 11, 16, 22-25, 38, 39), is realized especially by the HPC and ERC of the hippocampal complex. However, given that these two regions perform distinct functions, with the ERC encoding continuous space discretely (16) and the HPC represent localized spatial locations (2), a longstanding puzzle is to understand how these two regions work collaboratively in navigation. With the object-matching task that was able to track HPC activity based on movement directions while controlling movement distance, we identified a 3-fold spatial periodicity in the HPC, which was cross-validated through sinusoidal and spectral analyses and replicated by two independent groups of human participants. Critically, the 3-fold periodicity in the HPC was synchronized in phase with the 6-fold periodicity in the ERC with no peak offset, which was further embedded in the behavioral performance of navigation. In summary, our findings suggest a potential mechanism of the spatial periodic computation of hippocampus-entorhinal circuit in navigation, which eventually influenced the visual-motor system and resulted in behavioral periodicity during navigation.

Previous navigational models (e.g., 21, 40-42) heavily rely on simulations of hippocampal and entorhinal cells. However, the computational principles governing how these cells operate collaboratively as an integrated whole are not fully understood. Our fMRI experiment provides reliable empirical evidence suggesting a possible mechanism of spatial periodic computation, which may embed spatial orientations and path directions within a periodic scaffold defined by 3-fold spatial periodicity and spatial phase (i.e., grid orientation). Furthermore, the finding that the behavioral periodicity in navigation is phase-coupled with the hippocampal periodicity suggests that this periodic scaffold may extend its function to downstream cortical regions beyond the MTL (see also 43). In parallel, neurons exhibiting spatial selectivity in upstream cortical regions, possibly first reported by Hubel and Wiesel (44, 45) for the ganglion cells in representing visual locations, may also provide external visual cues with local geometry to the HPC, especially when allocentric map is not accessible (39, 46). Taken together, the principle of spatial periodic computation may serve as a general rule for structuring information in both spatial and

temporal domains throughout the brain, possibly facilitating how information is organized, stored, and retrieved as a structured entity.

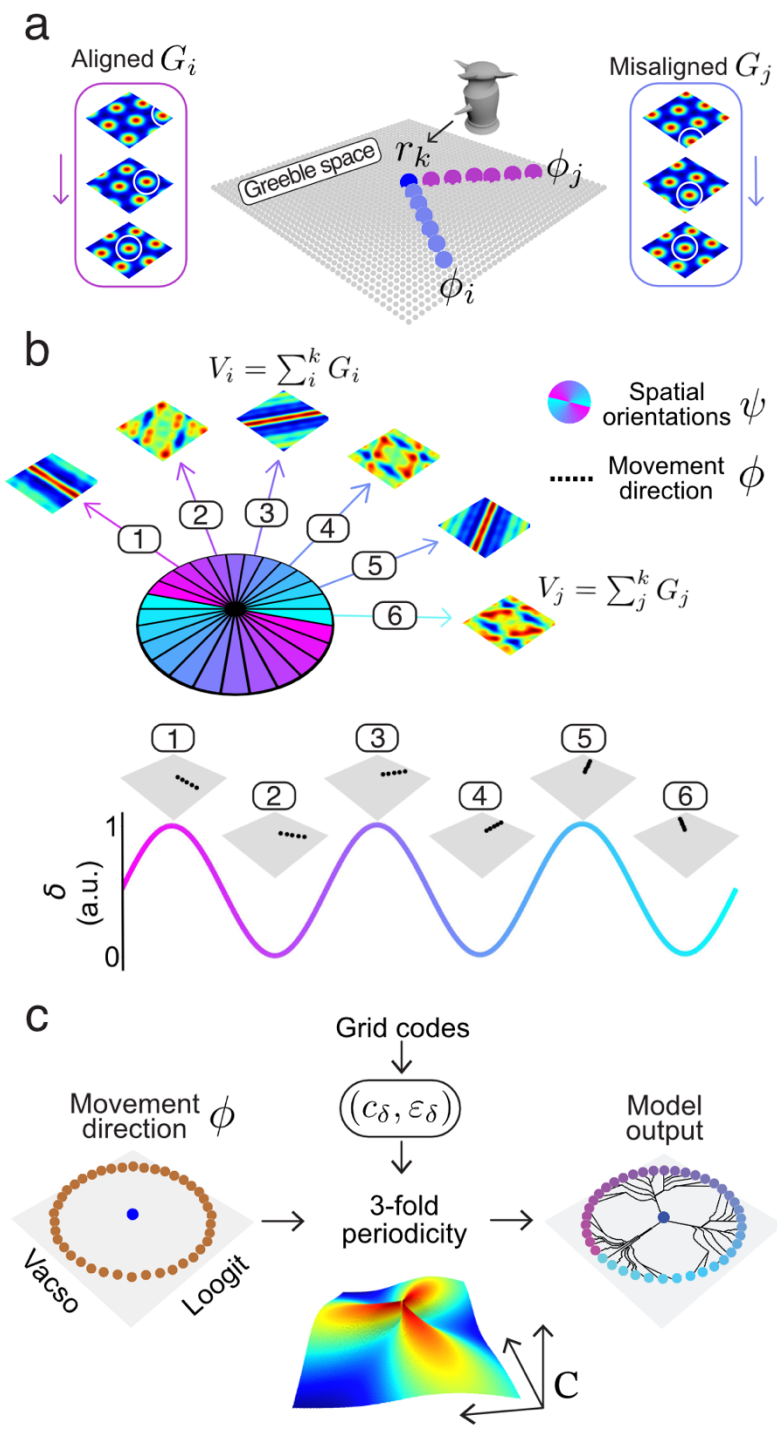

Fig. 6. The E-H PhaseSync Model. a) Discrete locations encoded by grid cells. Paths from the starting-location r_i and r_j to the goal-location r_k in the greeble space are mentally planed by imagination, illustrating alignments and misalignments of their movement directions relative to grid axes, respectively. Grid cells associated with the locations along

the paths are activated through mental imagination. b) Hypothetical algorithm of the formation of 3-fold periodicity in the HPC. First, path code V is formed by integrating the 2D space codes of activated grid cells. V is symmetrical for movement direction ϕ and ϕ+180°, representing a unique spatial orientation ψ ranged from 0° to 180°. Second, the neural representation δ of spatial orientation indicates the extent to which a movement direction ϕ aligns with grid axes. The largest δ value, indicating a perfect match between ϕ and grid axes (e.g., the spatial orientation 1 3 5). In contrast, a weaker δ value results from a mismatch between ϕ and grid axes (e.g., the spatial orientation 2 4 6), thus exhibiting a 3-fold periodicity. c) Model simulation in the greeble space. The vector representation C of the HPC was computed for each location of the greeble space using a cosine function, where the parameters (i.e., spatial frequency c_δ and phase ε_δ) were inherited from δ periodicity. The model receives the self-location an input and output the next location based on winner-take-all dynamics (17-21). Each movement was made with an initial step size of 1 pixel. The color scale of starting-locations denotes movement directions ranging from 0° to 360°.

Based on this hypothesis, we proposed a cognitive model, coined the E-H PhaseSync model (Fig.6), to elucidate the possibility that how the 3-fold periodicity was generated by populational neurons within the ERC-HPC circuit and its role in supporting the encoding of movement directions by hippocampal place cells (11, 47-51). In this model, a path code for each starting location was generated by activating grid cell population, possibly corresponding to the "planar waves" proposed by theoretical models (26, 52), which encode locations within a path during mental imagination. Specifically, the path code for a movement direction is likely identical to that of its reverse direction, as empirical evidence from the reorientation studies (39, 46, 53, 54) shows that rodents and young children tend to search for targets equally at two geometrically equivalent opposite locations. Thus, the path codes serve as a periodic scaffold, with their phases tightly coupled with the three main axes of grid cells, providing formation for movement directions during navigation. For details of the model and simulation, see fig.6 legend and Supplementary text.

A key component of this model is the path code, which acts as a bridge between the global spatial metric of entorhinal grid cells and the local movement directions of hippocampal place cells. Specifically, this component transforms spatial metric encoded in an abstract cognitive map into movement directions in an actual one, hereby enabling agents' navigation in both physical and conceptual spaces. The path code in the model aligns nicely with the planar waves from the "grid cell to place cell" model (17-21), the oscillatory interference theory (52), and the concept of the spatially periodic bands (26). In addition, it offers an explanation for the observation of irregular trace fields (55) by suggesting the cause of the misalignment between the primary axes of grid cells and path directions encoded by place cells.

While the E-H PhaseSync model holds promising as a cognitive model, there is a notable lack of direct neural evidence supporting it, especially concerning the path code. The recent discovery of vector trace cells in the subiculum (55), which help forming a vector or gradient path from one location to another, suggests a potential neural basis for the path code. Further neurophysiological investigations are needed to unveil their exact role and mechanism. Another limitation of this model relies solely on the afferent connection from the ERC to the HPC and does not consider the reverse signal transmission from the HPC to the ERC (56, 57). In addition, we also discovered the 3-fold periodicity in the default mode network and the HG in the whole-brain analysis, suggesting that the spatial periodic computation may operate beyond the hippocampus-entorhinal circuit that our model focuses on.

Finally, our model does not elucidate how hippocampal vector fields update in response to unexpected landmark or obstacles. Previous studies suggest that the ERC may receive contextual information and updated goal identities (e.g., intermediate landmarks) from the parahippocampal and perirhinal cortices (58) and then integrate it into environmental metric (59) through the excitation-inhibition dynamics (60). Thus, further biologically plausible models, which explore interactive principles of various cognitive maps that flexibly organize past experiences for the future (61), are needed to provide further insights how these maps contribute to a unified and efficient representation of the external world.

545

STAR Methods

Participants

Two groups of twenty right-handed university students with normal or corrected-to-normal vision were recruited for this study. The first group, referred to as the experimental group, consisted of ten students from Peking University. The second group, aimed at replicating the study, included ten students from Tsinghua University. The age and sex of the participants were balanced across both groups (experimental group: mean age = 22.10 [SD = 2.23], 5 females, 5 males; replication group: mean age = 23.9 [SD = 3.51], 5 females, 5 males). All participants had no history of psychiatric or neurological disorders and gave their written informed consent prior to the experiment, which received approval from the Research Ethics Committee of both universities.

Experimental design

Artificial greeble space. The greebles (32) were generated using Autodesk 3ds Max (version 2022, http://www.autodesk.com), with the MAXScript codes from the TarrLab stimulus datasets (http://www.tarrlab.org/). A greeble's identity was determined by the lengths of two distinct features, arbitrarily named as "Loogit" and "Vacso" (Fig.1a). These names were unrelated to the object matching task. The greebles were arranged in a 45-by-45 matrix, forming a two-dimensional space, with each greeble representing a location. The 'Loogit' feature length corresponded to the y-axis, and the 'Vacso' feature length to the x-axis (Fig. 1c). The prototype greeble, marked by a blue dot in Fig.1c, was positioned at the center of this space and had equal lengths of Loogit and Vacso. This prototype served as the target for the task. The ratio of each greeble's feature length relative to the prototype was ranged from 0.12 to 1.88, with a step size of 0.04, providing a smooth morphing experience as participants adjusted the lengths of the greeble features.

Experimental design. The object matching task was programmed by Python (version 3.9) and utilized Pygame (version 2.0, https://www.pygame.org/), a library designed for developing video games. Each trial began with a 2.0-s fixation screen, followed by the presentation of a pseudo-randomly selected greeble variant from those near the boundary of the space (orange dots in Fig.1c), centered on the screen (Fig.1b). Participants were tasked with adjusting the lengths of this variant to match a prototype as quickly as possible

by pressing buttons. Two response boxes enabled participants to stretch or shrink the two greeble features. These boxes were counterbalanced between the left and right hands of participants. To mitigate the impact of learning effects on the BOLD signal of movement directions during MRI scanning, participants underwent training one day prior to the MRI experiment. On day 1, participants adjusted the variant's lengths in a self-paced manner by pressing the return key to end the trial. Feedback was provided after each trial in the first 7 sessions (e.g., "Loogit: 5 percent longer than the target"), but the 8th session offered no feedback to assess behavioral performance. Before starting, participants familiarized themselves with the prototype through observation and completed at least 10 practice trials with feedback. Day 2's procedure mirrored day 1, except that (1) participant's response in each trial has a 10-s time limit. A timer was presented on top of screen (Fig.1b), (2) no feedback was provided, and (3) the completion of the task in an MRI scanner. Consequently, learning effects were not observed during the MRI scanning on day 2 (Fig.S1), and were only apparent during the practice session on day 1. The task was designed to cover the potential movement directions evenly; therefore, 24 variants were pseudo-randomly selected from each 30° bin of the ring, with an angular precision of 1°, resulting in 288 variants. These variants were distributed across 8 experimental sessions, each containing 36 object matching trials and 4 lure trials. The lure trial presented a blank screen after the fixation for 10 seconds. The totaling 320 trials lasted approximately one hour. Participants were incentivized to perform accurately with the promise of exponentially increasing monetary compensation based on their performance. Post-scan, participants were debriefed, shown their performance results, and asked to discuss their subjective experience and reasons for any performance issues. Importantly, participants were unaware of the concept of greeble space or the spatial feature adjustments involved in the experiment.

fMRI data acquisition

Imaging data were collected using a 3T Siemens Prisma scanner, equipped with a 64- and 20-channel receiver head coil for the experimental and replication groups, respectively, at the PKU and Tsinghua Imaging Center. Functional data were acquired with a Multi-band Echo Planer imaging (EPI) sequence with the following parameters: Acceleration Factor:

608 2, TR = 2000 ms, TE = 30 ms, matrix size = 112 × 112 x 62, flip angle = 90°, resolution =
609 2 × 2 × 2.3 mm^3, 62 slices with a slice thickness of 2 mm and a gap of 0.3 mm, in a
610 transversal slice orientation. Additionally, high-resolution T1-weighted three-dimensional
611 anatomical datasets were collected for registration purposes using MPRAGE sequences,
612 detailed as follows: TR = 2530 ms, TE = 2.98 ms, matrix size = 448 x 512 x 192, flip angle
613 = 7°, resolution = 0.5 × 0.5 × 1 mm^3, 192 slices with a slice thickness of 1 mm, in a sagittal
614 slice orientation. In the experimental group, stimuli were presented through a Sinorad LCD
615 projector (Shenzhen Sinorad Medical Electronics) onto a 33-inch rear-projection screen.
616 For the replication group, stimuli presentation was managed using a visual/audio
617 stimulation system (Shenzhen Sinorad SA-9939) and an MRI-compatible 40-inch LED
618 liquid crystal display, custom-designed by Shenzhen Sinorad Medical Electronics Co., Ltd.
619 The screen resolution for both groups was 1024 x 768, and participants viewed the stimuli
620 through an angled mirror mounted on the head coil.
621
622 **fMRI data preprocessing**
623 The BOLD signal series from each scan session was preprocessed independently using the
624 FSL FEAT toolbox from the FMRIB's Software Library (version 6.0,
625 https://fsl.fmrib.ox.ac.uk/fsl/fslwiki)(62-64). For each of eight scan sessions, the BOLD
626 signal series were corrected for motion artifacts, slice time acquisition differences,
627 geometrical distortion with fieldmaps, and were applied with a high-pass filter with a cutoff
628 of 100 seconds. Spatial smoothing was then performed using a Gaussian kernel with a full
629 width at half maximum (FWHM) of 5 mm. For group-level analysis, the preprocessed
630 BOLD signal series were registered to each participant's high-resolution anatomical image
631 and further normalized to the standard MNI152 image using FSL FLIRT (65). This
632 normalization step also involved resampling the functional voxels to a resolution of 2 x 2
633 x 2 mm.
634
635 **Sinusoidal analysis**
636 Sinusoidal analysis was employed to investigate the 6-fold hexagonal activity of the ERC
637 during the object matching task, following previously established protocols (27-31). First,
638 we computed the grid orientation for each participant from the ERC using one half of the

data (odd-numbered sessions: 1, 3, 5, 7). Second, the neural representation of the hexagonal activity, modulated by the movement directions ranged from 0° to 360° relative to the goal-location in the greeble space, were examined with grid orientation controlled. Specifically, a GLM was firstly created for each session to model the BOLD signals of the ERC convolved with FSL Double-Gamma hemodynamic response function using two parametric modulators: sin(6θ) and cos(6θ), where θ represents the movement directions, while the factor "6" represents the rotationally symmetric 6-fold neural activity. The factor "4", "5" and "7" were used as control parameters, these parameters misalign with the primary axes of grid cells. Second, the estimated weights β_{sine} and β_{cosine} were used to compute the grid orientation φ, ranged from 0° to 59°, in each voxel, session, and participant, where $\varphi = [\arctan(\frac{\beta_{sine}}{\beta_{cosine}})]/6$. The φ maps of each participant were averaged across the odd-numbered sessions, and were further averaged across the voxels in the ERC, resulting a value Φ representing the grid orientation for the participant. Third, another GLM, fitted to model the BOLD signal series of the other half of the data (even-numbered sessions: 2,4,6,8), was specified with a cosine parametric modulator, cos(6[θ - Φ]), to examine the hexagonal activity using the movement directions calibrated by the grid orientation. Forth, the hexagonal activity map was derived for each participant through averaging the weight map of the cosine modulator across the even-numbered sessions, which was further converted to z-score map before submitting to second-level analysis (66).

Spectral analysis of MRI BOLD signals

Spectral analysis was employed to examine the spatial periodicity in the BOLD signals of the HPC. First, a GLM was created to extract activity maps corresponding to movement directions in the greeble space. Specifically, these directions, represented by paths from starting-locations to the ending-locations, were down-sampled into 15° bins (e.g., the movement directions ranging from -7.5° to 7.5° were labeled as 0°; and those from 337.5° to 352.5° were labeled as 345°). This process resulted in a vector of 24 resampled movement directions (i.e., the number of bins), providing sufficient sample size for spectral analysis (67). The BOLD signals from each voxel were then modelled using a GLM, with the 24 directional bins as parametric modulators. This yielded 24 direction-dependent activity maps for each participant, which were sorted in ascending order (i.e., from 0° to

360°) and detrended. Second, these direction-based activities were transformed from the spatial domain to the frequency domain using the Fast Discrete Fourier Transform (FFT) (implemented in the stats package of R platform, version 4.0, https://www.r-project.org/)(68). The spectral magnitude was calculated from the absolute values of the FFT output for each of 0- to 11-fold. Forth, this analysis produced brain maps of spectrum magnitude for each voxel, spatial fold, and participant. The 99th percentile of the pseudo t-statistic distribution, calculated as the mean spectral magnitude divided by the standard error across participants, was used as the initial threshold before performing the group-level correction for multiple comparisons.

Spectral analysis of human behavior

Participants' behavioral periodicity was examined using spectral analysis, following the save methodology as that used for BOLD signal periodicity. Specifically, we first calculated a navigation efficiency score for each trial of each participant, using the formula by $T - T' + E/0.04$, where T and T' represent the actual and theoretically optimized path length, respectively. These lengths were defined by the number of movement step in pixels required to reach the goal. E quantifies the error size, measured by the distance between the participant's ending-locations and the goal-location in the unit of ratio. The constant "0.04", which is the step size of the ratio of greeble features relative to the greeble prototype, converts the units of E from greeble feature ratios to pixel space. The adjustment for the theoretically optimized path length addresses the confounding effect of path length biases between the cardinal directions (i.e., "East", "South", "West", and "North") and the intercardinal directions (e.g., "Southeast"). Specifically, a path directed "East" is inherently shorter than one directed "Southeast". To counter this bias, we computed the theoretically shortest path length for each trial, subtracting this from the participant's actual path length. This approach isolates the pure behavioral bias in movement directions. High navigation efficiency is characterized by shorter paths and smaller errors. This method produces a vector of navigation efficiencies as a function of movement directions for each participant. Movement direction for each trial was determined by the vector from the participant's starting to ending location. Subsequently, each participant's efficiency vector was down-sampled using 10° bins, resulting in a resampled vector of 36 sample points, which were

701 further subjected to spectral analysis, employing the same procedure used for analyzing
702 BOLD signal periodicity.
703
704 **Anatomical masks**
705 The mask for the bilateral ERC was manually delineated on the MNI T1 brain with 1 mm
706 resolution packaged by FSL, using established protocols (69), and the delineation software
707 ITK-SNAP (Version 3.8, www.itksnap.org). The mask for the bilateral HPC were derived
708 from an automated anatomical parcellation of the spatially normalized single-subject high-
709 resolution T1 volume, as provided by the Montreal Neurological Institute (MNI)(Version:
710 AAL3, https://www.gin.cnrs.fr/en/tools/aal/)(33). All masks were then resampled to a 2
711 mm resolution and aligned with the standard MNI space.
712
713 **Statistical analysis**
714 The periodicity of the BOLD signal was analyzed using cluster-based permutation methods
715 provided by FSL randomise (version 2.9, http://fsl.fmrib.ox.ac.uk/fsl/fslwiki/Randomise).
716 Initially, uncorrected clusters were derived using a threshold of $p < 0.01$ based on a two-
717 tailed t-test for sinusoidal analysis, and a one-tailed t test for spectral analysis. If no clusters
718 emerged, a more liberal threshold of $p < 0.05$ was employed. The reliability of these
719 uncorrected clusters was assessed using a non-parametric statistical inference, which does
720 not rely on assumptions about data distribution (70). Specifically, 5,000 random sign-flips
721 were performed on the sinusoidal beta or FFT magnitude images. Clusters exceeding 95%
722 of the maximal suprathreshold cluster size from the permutation distribution were
723 considered significant. The periodicity of behavioral navigation efficiency, calculated from
724 human participants, was examined using FFT. The initial threshold of each periodic fold
725 was set at the 99th percentile of the shuffled magnitude distribution, with the corrected
726 threshold for multiple comparison derived from the maximum of these initial thresholds
727 across all periodic folds. Coherence between the BOLD signals of the ERC and HPC was
728 analyzed using the amplitude-phase coupling analysis (34), without applying a band-pass
729 filter. Similarly, the coherence between the HPC BOLD signal and participant's navigation
730 efficiency was assessed using the phase-lag index (71), also without a band-pass filter. The
731 robustness of the observed coherence was evaluated by a permutation test involving 5000

shuffles of the movement directions, with significance defined as exceeding the 99th percentile of the shuffled distribution.

References

1. Tolman, E. C. (1948). Cognitive maps in rats and men. Psychol Rev, 55(4), 189-208.
2. O'Keefe, J., & Dostrovsky, J. (1971). The hippocampus as a spatial map: preliminary evidence from unit activity in the freely-moving rat. Brain research.
3. Epstein, R. A., Patai, E. Z., Julian, J. B., & Spiers, H. J. (2017). The cognitive map in humans: spatial navigation and beyond. Nature neuroscience, 20(11), 1504-1513.
4. Behrens, T. E., Muller, T. H., Whittington, J. C., Mark, S., Baram, A. B., Stachenfeld, K. L., & Kurth-Nelson, Z. (2018). What is a cognitive map? Organizing knowledge for flexible behavior. Neuron, 100(2), 490-509.
5. Bottini, R., & Doeller, C. F. (2020). Knowledge across reference frames: Cognitive maps and image spaces. Trends in Cognitive Sciences, 24(8), 606-619.
6. Park, S. A., Miller, D. S., Nili, H., Ranganath, C., & Boorman, E. D. (2020). Map making: constructing, combining, and inferring on abstract cognitive maps. Neuron, 107(6), 1226-1238.
7. Toledo, S., Shohami, D., Schiffner, I., Lourie, E., Orchan, Y., Bartan, Y., & Nathan, R. (2020). Cognitive map–based navigation in wild bats revealed by a new high-throughput tracking system. Science, 369(6500), 188-193.
8. Nyberg, N., Duvelle, É., Barry, C., & Spiers, H. J. (2022). Spatial goal coding in the hippocampal formation. Neuron.
9. De Cothi, W., Nyberg, N., Griesbauer, E. M., Ghanamé, C., Zisch, F., Lefort, J. M., ... & Spiers, H. J. (2022). Predictive maps in rats and humans for spatial navigation. Current Biology, 32(17), 3676-3689.
10. Muhle-Karbe, P. S., Sheahan, H., Pezzulo, G., Spiers, H. J., Chien, S., Schuck, N. W., & Summerfield, C. (2023). Goal-seeking compresses neural codes for space in the human hippocampus and orbitofrontal cortex. Neuron.
11. Ormond, J., & O'Keefe, J. (2022). Hippocampal place cells have goal-oriented vector fields during navigation. Nature, 607(7920), 741-746.

12. Witter, M. P., & Amaral, D. G. (1991). Entorhinal cortex of the monkey: V. Projections to the dentate gyrus, hippocampus, and subicular complex. J Comp Neurol, 307(3), 437-459.
13. van Groen, T., Miettinen, P., & Kadish, I. (2003). The entorhinal cortex of the mouse: organization of the projection to the hippocampal formation. Hippocampus, 13(1), 133-149.
14. Garcia, A. D., & Buffalo, E. A. (2020). Anatomy and function of the primate entorhinal cortex. Annual Review of Vision Science, 6, 411-432.
15. Hales, J. B., Schlesiger, M. I., Leutgeb, J. K., Squire, L. R., Leutgeb, S., & Clark, R. E. (2014). Medial entorhinal cortex lesions only partially disrupt hippocampal place cells and hippocampus-dependent place memory. Cell reports, 9(3), 893-901.
16. Hafting, T., Fyhn, M., Molden, S., Moser, M. B., & Moser, E. I. (2005). Microstructure of a spatial map in the entorhinal cortex. Nature, 436(7052), 801-806.
17. Solstad, T., Moser, E. I., & Einevoll, G. T. (2006). From grid cells to place cells: a mathematical model. Hippocampus, 16(12), 1026-1031.
18. De Almeida, L., Idiart, M., & Lisman, J. E. (2009). The input–output transformation of the hippocampal granule cells: from grid cells to place fields. Journal of Neuroscience, 29(23), 7504-7512.
19. Bush, D., Barry, C., & Burgess, N. (2014). What do grid cells contribute to place cell firing? Trends Neurosci, 37(3), 136-145.
20. Bush, D., Barry, C., Manson, D., & Burgess, N. (2015). Using grid cells for navigation. Neuron, 87(3), 507-520.
21. Bicanski, A., & Burgess, N. (2019). A computational model of visual recognition memory via grid cells. Current Biology, 29(6), 979-990.
22. Sargolini, F., Fyhn, M., Hafting, T., McNaughton, B. L., Witter, M. P., Moser, M. B., & Moser, E. I. (2006). Conjunctive representation of position, direction, and velocity in entorhinal cortex. Science, 312(5774), 758-762.
23. Munn, R. G., Mallory, C. S., Hardcastle, K., Chetkovich, D. M., & Giocomo, L. M. (2020). Entorhinal velocity signals reflect environmental geometry. Nature neuroscience, 23(2), 239-251.

24. Gerlei, K., Passlack, J., Hawes, I., Vandrey, B., Stevens, H., Papastathopoulos, I., & Nolan, M. F. (2020). Grid cells are modulated by local head direction. Nature communications, 11(1), 4228.
25. Gardner, R. J., Hermansen, E., Pachitariu, M., Burak, Y., Baas, N. A., Dunn, B. A., ... & Moser, E. I. (2022). Toroidal topology of population activity in grid cells. Nature, 602(7895), 123-128.
26. Krupic, J., Burgess, N., & O'Keefe, J. (2012). Neural representations of location composed of spatially periodic bands. Science, 337(6096), 853-857.
27. Doeller, C. F., Barry, C., & Burgess, N. (2010). Evidence for grid cells in a human memory network. Nature, 463(7281), 657-661.
28. Constantinescu, A. O., O'Reilly, J. X., & Behrens, T. E. J. (2016). Organizing conceptual knowledge in humans with a gridlike code. Science, 352(6292), 1464-1468.
29. Bao, X., Gjorgieva, E., Shanahan, L. K., Howard, J. D., Kahnt, T., & Gottfried, J. A. (2019). Grid-like Neural Representations Support Olfactory Navigation of a Two-Dimensional Odor Space. Neuron, 102(5), 1066-1075 e1065.
30. Wagner, I. C., Graichen, L. P., Todorova, B., Lüttig, A., Omer, D. B., Stangl, M., & Lamm, C. (2023). Entorhinal grid-like codes and time-locked network dynamics track others navigating through space. Nature Communications, 14(1), 231.
31. Raithel, C. U., Miller, A. J., Epstein, R. A., Kahnt, T., & Gottfried, J. A. (2023). Recruitment of grid-like responses in human entorhinal and piriform cortices by odor landmark-based navigation. Current Biology, 33(17), 3561-3570.
32. Gauthier, I., & Tarr, M. J. (1997). Becoming a "Greeble" expert: exploring mechanisms for face recognition. Vision Res, 37(12), 1673-1682.
33. Rolls, E. T., Huang, C. C., Lin, C. P., Feng, J., & Joliot, M. (2020). Automated anatomical labelling atlas 3. Neuroimage, 206, 116189.
34. Canolty, R. T., Edwards, E., Dalal, S. S., Soltani, M., Nagarajan, S. S., Kirsch, H. E., ... & Knight, R. T. (2006). High gamma power is phase-locked to theta oscillations in human neocortex. science, 313(5793), 1626-1628.
35. Buzsaki, G. (2006). Rhythms of the Brain. Oxford university press.

36. Maris, E., van Vugt, M., & Kahana, M. (2011). Spatially distributed patterns of oscillatory coupling between high-frequency amplitudes and low-frequency phases in human iEEG. Neuroimage, 54(2), 836-850.
37. Friese, U., Köster, M., Hassler, U., Martens, U., Trujillo-Barreto, N., & Gruber, T. (2013). Successful memory encoding is associated with increased cross-frequency coupling between frontal theta and posterior gamma oscillations in human scalp-recorded EEG. Neuroimage, 66, 642-647.
38. Wang, R. F., & Spelke, E. S. (2002). Human spatial representation: Insights from animals. Trends in cognitive sciences, 6(9), 376-382.
39. Gallistel, C. R. (2017). Navigation: whence our sense of direction?. Current Biology, 27(3), R108-R110.
40. Gao, R., Xie, J., Zhu, S. C., & Wu, Y. N. (2018). Learning Grid Cells as Vector Representation of Self-Position Coupled with Matrix Representation of Self-Motion. In International Conference on Learning Representations.
41. Whittington, J. C., Muller, T. H., Mark, S., Chen, G., Barry, C., Burgess, N., & Behrens, T. E. (2020). The Tolman-Eichenbaum machine: unifying space and relational memory through generalization in the hippocampal formation. Cell, 183(5), 1249-1263.
42. Edvardsen, V., Bicanski, A., & Burgess, N. (2020). Navigating with grid and place cells in cluttered environments. Hippocampus, 30(3), 220-232.
43. Fiebelkorn, I. C., Pinsk, M. A., & Kastner, S. (2018). A Dynamic Interplay within the Frontoparietal Network Underlies Rhythmic Spatial Attention. Neuron, 99(4), 842-853 e848.
44. Hubel, D. H., & Wiesel, T. N. (1959). Receptive fields of single neurones in the cat's striate cortex. J Physiol, 148, 574-591.
45. Hubel, D. H., & Wiesel, T. N. (1962). Receptive fields, binocular interaction and functional architecture in the cat's visual cortex. J Physiol, 160, 106-154.
46. Julian, J. B., Keinath, A. T., Marchette, S. A., & Epstein, R. A. (2018). The neurocognitive basis of spatial reorientation. Current Biology, 28(17), R1059-R1073.

47. Muller, R. U., Bostock, E., Taube, J. S., & Kubie, J. L. (1994). On the directional firing properties of hippocampal place cells. Journal of Neuroscience, 14(12), 7235-7251.
48. Leutgeb, S., Ragozzino, K. E., & Mizumori, S. J. (2000). Convergence of head direction and place information in the CA1 region of hippocampus. Neuroscience, 100(1), 11-19.
49. Rubin, A., Yartsev, M. M., & Ulanovsky, N. (2014). Encoding of head direction by hippocampal place cells in bats. Journal of Neuroscience, 34(3), 1067-1080.
50. Meister, M. L., & Buffalo, E. A. (2016). Getting directions from the hippocampus: The neural connection between looking and memory. Neurobiology of learning and memory, 134, 135-144.
51. Sarel, A., Finkelstein, A., Las, L., & Ulanovsky, N. (2017). Vectorial representation of spatial goals in the hippocampus of bats. Science, 355(6321), 176-180.
52. Welday, A. C., Shlifer, I. G., Bloom, M. L., Zhang, K., & Blair, H. T. (2011). Cosine directional tuning of theta cell burst frequencies: evidence for spatial coding by oscillatory interference. Journal of Neuroscience, 31(45), 16157-16176.
53. Hermer, L., & Spelke, E. S. (1994). A geometric process for spatial reorientation in young children. Nature, 370(6484), 57-59.
54. Julian, J. B., Keinath, A. T., Muzzio, I. A., & Epstein, R. A. (2015). Place recognition and heading retrieval are mediated by dissociable cognitive systems in mice. Proceedings of the National Academy of Sciences, 112(20), 6503-6508.
55. Poulter, S., Lee, S. A., Dachtler, J., Wills, T. J., & Lever, C. (2021). Vector trace cells in the subiculum of the hippocampal formation. Nature neuroscience, 24(2), 266-275.
56. Bonnevie, T., Dunn, B., Fyhn, M., Hafting, T., Derdikman, D., Kubie, J. L., ... & Moser, M. B. (2013). Grid cells require excitatory drive from the hippocampus. Nature neuroscience, 16(3), 309-317.
57. Dordek, Y., Soudry, D., Meir, R., & Derdikman, D. (2016). Extracting grid cell characteristics from place cell inputs using non-negative principal component analysis. Elife, 5, e10094.

58. Eichenbaum, H., & Lipton, P. A. (2008). Towards a functional organization of the medial temporal lobe memory system: role of the parahippocampal and medial entorhinal cortical areas. Hippocampus, 18(12), 1314-1324.
59. Stensola, T., Stensola, H., Moser, M. B., & Moser, E. I. (2015). Shearing-induced asymmetry in entorhinal grid cells. Nature, 518(7538), 207-212.
60. Fuhs, M. C., & Touretzky, D. S. (2006). A spin glass model of path integration in rat medial entorhinal cortex. Journal of Neuroscience, 26(16), 4266-4276.
61. Zhang, B., Ma, L., & Liu, J. (2023). Experience replay facilitates the formation of the hexagonal pattern of grid cells. bioRxiv, 2023-02.
62. Woolrich, M. W., Jbabdi, S., Patenaude, B., Chappell, M., Makni, S., Behrens, T., ... & Smith, S. M. (2009). Bayesian analysis of neuroimaging data in FSL. Neuroimage, 45(1), S173-S186.
63. Smith, S. M., Jenkinson, M., Woolrich, M. W., Beckmann, C. F., Behrens, T. E., Johansen-Berg, H., ... & Matthews, P. M. (2004). Advances in functional and structural MR image analysis and implementation as FSL. Neuroimage, 23, S208-S219.
64. Jenkinson, M., Beckmann, C. F., Behrens, T. E., Woolrich, M. W., & Smith, S. M. (2012). Fsl. Neuroimage, 62(2), 782-790.
65. Jenkinson, M., & Smith, S. (2001). A global optimisation method for robust affine registration of brain images. Med Image Anal, 5(2), 143-156.
66. Schlichting, M. L., Mumford, J. A., & Preston, A. R. (2015). Learning-related representational changes reveal dissociable integration and separation signatures in the hippocampus and prefrontal cortex. Nat Commun, 6, 8151.
67. De Valois, R. L., Albrecht, D. G., & Thorell, L. G. (1982). Spatial frequency selectivity of cells in macaque visual cortex. Vision Res, 22(5), 545-559.
68. Landau, A. N., & Fries, P. (2012). Attention samples stimuli rhythmically. Curr Biol, 22(11), 1000-1004.
69. Insausti, R., Juottonen, K., Soininen, H., Insausti, A. M., Partanen, K., Vainio, P., Laakso, M. P., & Pitkanen, A. (1998). MR volumetric analysis of the human entorhinal, perirhinal, and temporopolar cortices. AJNR Am J Neuroradiol, 19(4), 659-671.

70. Nichols, T. E., & Holmes, A. P. (2002). Nonparametric permutation tests for functional neuroimaging: a primer with examples. Hum Brain Mapp, 15(1), 1-25.
71. Stam, C. J., Nolte, G., & Daffertshofer, A. (2007). Phase lag index: assessment of functional connectivity from multi channel EEG and MEG with diminished bias from common sources. Human brain mapping, 28(11), 1178-1193.
72. Buckner, R. L. (2010). The role of the hippocampus in prediction and imagination. Annual review of psychology, 61, 27-48.
73. Mullally, S. L., & Maguire, E. A. (2014). Memory, imagination, and predicting the future: A common brain mechanism?. The Neuroscientist, 20(3), 220-234.
74. O'keefe, J., & Burgess, N. (2005). Dual phase and rate coding in hippocampal place cells: theoretical significance and relationship to entorhinal grid cells. Hippocampus, 15(7), 853-866.
75. Burgess, N., Barry, C., & O'Keefe, J. (2007). An oscillatory interference model of grid cell firing. Hippocampus, 17(9), 801-812.
76. Blair, H. T., Welday, A. C., & Zhang, K. (2007). Scale-invariant memory representations emerge from moire interference between grid fields that produce theta oscillations: a computational model. Journal of Neuroscience, 27(12), 3211-3229.
77. Bush, D., & Schmidt-Hieber, C. (2018). Computational models of grid cell firing. Hippocampal Microcircuits: A Computational Modeler's Resource Book, 585-613.
78. Kang, L., & Balasubramanian, V. (2019). A geometric attractor mechanism for self-organization of entorhinal grid modules. Elife, 8, e46687.
79. Stemmler, M., Mathis, A., & Herz, A. V. (2015). Connecting multiple spatial scales to decode the population activity of grid cells. Sci Adv, 1(11), e1500816.
80. Dragoi, G., & Tonegawa, S. (2011). Preplay of future place cell sequences by hippocampal cellular assemblies. Nature, 469(7330), 397-401.
81. Pfeiffer, B. E. (2020). The content of hippocampal “replay”. Hippocampus, 30(1), 6-18.

82. Woolrich, M. W., Ripley, B. D., Brady, M., & Smith, S. M. (2001). Temporal autocorrelation in univariate linear modeling of FMRI data. Neuroimage, 14(6), 1370-1386.

Acknowledgments

We gratefully acknowledge Yue Wu, Yuannan Li, and Ao Li for their insightful discussions during data analysis. We also thank Russell Epstein for his valuable comments on fMRI analysis and computational modeling, and Dr. Michael Tarr for sharing the code for Greeble stimulus generation. Computational work was supported by the High-performance Computing Platform of Peking University.

Funding

The work was supported by the following funding sources:
National Key R&D Program of China 2020AAA0105200 (J.L.)
China Postdoctoral Science Foundation 2022M710470 (B.Z.)
Beijing Municipal Science & Technology Commission & Administrative Commission of Zhongguancun Science Park Z221100002722012 (J.L.)
Tsinghua University Guoqiang Institute 2020GQG1016 (J.L.)
Beijing Academy of Artificial Intelligence (J.L.).

Author contributions

Conceptualization: J.L.
Methodology: B.Z.
Investigation: B.Z.
Visualization: B.Z.
Resources: J.L.
Data Curation: B.Z.
Writing—Original Draft: B.Z., J.L.
Writing—Review & Editing: B.Z., J.L.
Project Administration: J.L.
Funding Acquisition: J.L.

Supervision: J.L.

Competing interests

None declared

Data and materials availability

All analyses reported in this study were conducted using customized codes written in Python (version 3.9), Pygame (version 2.0), Matlab (version 2019b), R (version 4.0), and GNU Bash (version 3.2.57). The codes are available from the corresponding author (J.L.) upon request. The neuroimaging toolbox and machine learning framework used in this work are publicly available as follows: FreeSurfer (version 7.1, https://surfer.nmr.mgh.harvard.edu/), FSL (version 6.0, https://fsl.fmrib.ox.ac.uk/fsl/fslwiki), and Torch (version 1.9, https://pytorch.org/). The MRI dataset and behavioral records from this study are publicly accessible at the Science Data Bank (https://doi.org/10.57760/sciencedb.18351). The original code of the "E-H PhaseSync" model is available from the open-access repository (https://github.com/ZHANGneuro/The-E-H-PhaseSync-Model).

Supplemental information

The spatial periodic computation of hippocampus-entorhinal circuit in navigation

Bo Zhang and Jia Liu

*Corresponding author. Email: liujiathu@tsinghua.edu.cn

This PDF file includes:

- Supplementary text
- Figs. S1 to S9

s

Supplementary text

The "E-H PhaseSync" Model

To elucidate the mechanism by which the hexagonal patterns of entorhinal grid cells project onto the HPC, giving rise to the 3-fold periodicity that guides navigation, we proposed a computational model, termed the "E-H PhaseSync" model. This model is predicated on an intuition that the 3-fold periodicity originates from the three primary axes of the hexagonal firing pattern of grid cells. This intuition is inspired by three factors. First, the ERC serves as one of the major projections of the HPC (12-14), lesion of the ERC results in abnormal spatial representation of the HPC (15). Second, grid cell population in the ERC show nearly invariant spatial orientation and spacing (16, 25). Third, the process of imagination has the capacity to activate a series of grid cells associated with the locations in planned path even without actual physical movement (72, 73). Therefore, the downstream HPC may therefore receive the conjunctive grid codes, and show the activity periodicity modulated by the grid axes.

A 45-by-45-pixel space, identical in size to the greeble space used in the object matching task, was simulated using Python (version 3.9), where each location (out of 2025 pixels) is denoted by coordinate vector $r = (x, y)$. The goal-location is situated at the center of the space, $r = (22,22)$. Grid cells are simulated using the cosine grating model (74-77). For each individual grid cell, the spatial code G is generated by summing three cosine gratings under the spatial phase $c_{(x,y)}$(Equation 1). The cosine gratings are oriented by the rotation vector k with 60° apart from one another. The parameter A represents the amplitude of cosine gratings. To simulate multi-scale encoding, the scale ratio of grid modules ω is defined at approximately 1.4 (78, 79). A total of 2025 (45-by-45 pixels) grid cells are generated for each module. All grid cells maintain a constant grid orientation, while grid phases vary, with each phase tied to a specific spatial location.

$$G_r = \sum_{i=1}^{3} A \cos(\omega_i (k_{i,x}(r_x - c_x) + k_{i,y}(r_y - c_y))) \quad (1)$$

The path code V is defined as the linear combination of grid codes exp $(\sum_i^k G_i)$ along a path (Fig.6b), where G represents the grid code, and i and k represent the starting- and goal-location, respectively. This process was inspired by the phenomena of

"imagination" (72,73) and "forward replay" (80-82) in the HPC. In these phenomena, an individual place cell triggers a sequence of spatially adjacent place cells, thereby activating corresponding grid cells that encode locations along the path.

$$V_i = \sum_i^k G_i \tag{2}$$

Note that when movement direction ϕ_i perfectly aligns with one of the primary axes of grid cells (i.e., spatial orientation $\boxed{1}\boxed{3}\boxed{5}$), path code V_i exhibits a "planar wave" pattern (26, 52), whereas when misaligned, the primary axes of grid cells deviate from the movement direction ϕ (i.e., spatial orientation $\boxed{2}\boxed{4}\boxed{6}$), resulting in an irregular multi-peak pattern V_j. The path code V are exactly identical for the movement direction ϕ and the direction ϕ + 180° (Fig.6b). These symmetrical patterns naturally reflect the spatial orientation ψ of the greeble space. In other words, the greeble space could be seen as a 1D vector of orientations ranged from 0 to π. The neural representation of spatial orientations was simulated by vector δ (Equation 3), where each orientation ψ was represented by a δ value calculated as the maximum of the sum of the location activity derived from the path code. R represents the location vector associated with the orientation ψ.

$$\delta = \left\{\sum_R V_{R,\psi}\right\}_{\psi=0}^{\pi} \tag{3}$$

The δ values index the degree of alignment between movement direction ϕ and the primary axes of grid cells. A large δ value indicates a close match, whereas a small δ value indicates a deviation of ϕ from grid axes. This process generated a 3-fold scaffold (Fig. 6b; bottom), characterized by the "aligned, deviated; aligned, deviated; aligned, deviated" pattern. This pattern is characterized by the 3-fold periodicity c_δ and the spatial phase ε_δ inherited from grid orientation. These two parameters were further used to generate the directional representation as described in Equation 4. $C_{dir,j}$ at location r_j is calculated based on the movement direction ϕ_j (Fig.6c; Left), defined by $\arctan\left(\frac{r'_y}{r'_x}\right)$, from r_j to the goal-location r_k, where r'_x and r'_y denote the relative distance in x and y domain between self- and goal-location, respectively.

$$C_{dir} = \cos\left(c_\delta \times \arctan(\phi_j) + \varepsilon_\delta\right) \tag{4}$$

Finally, the vector representation C in the HPC is generated by linearly integrating the directional representation C_{dir} and the distance representation C_{dis} (Fig.6c; Middle). C_{dis}, calculated from $\sqrt{r'^2_x + r'^2_y}$, is insensitive to spatial directions but signifies the distance between the current location and the goal-location, with larger C_{dis} value indicating a shorter distance to the goal.

During simulation, a total of 156 locations, forming a ring-shaped pattern near the boundary of the space, serve as starting-locations. In each movement step, a vector of HPC activity in the locations surrounding the self-location is extracted from C. Each movement transition is indicated by the location showing the strongest activity of the vector, conforming to winner-take-all dynamics (17-21). The step size is adjusted using a stepwise approach. The step size is initialized set to 1 pixel, and it is increased by 1 pixel if no stronger activity is found in the surrounding locations. The path length is computed by summing the distances between each pair of locations (current and next location). The path lengths are sorted by movement directions in ascending order before submitting to spectral analysis. The result showed a 3-fold periodicity, indicating that the path lengths changed as a function of movement directions (Fig.6c; Right).

Figs. S1 to S9

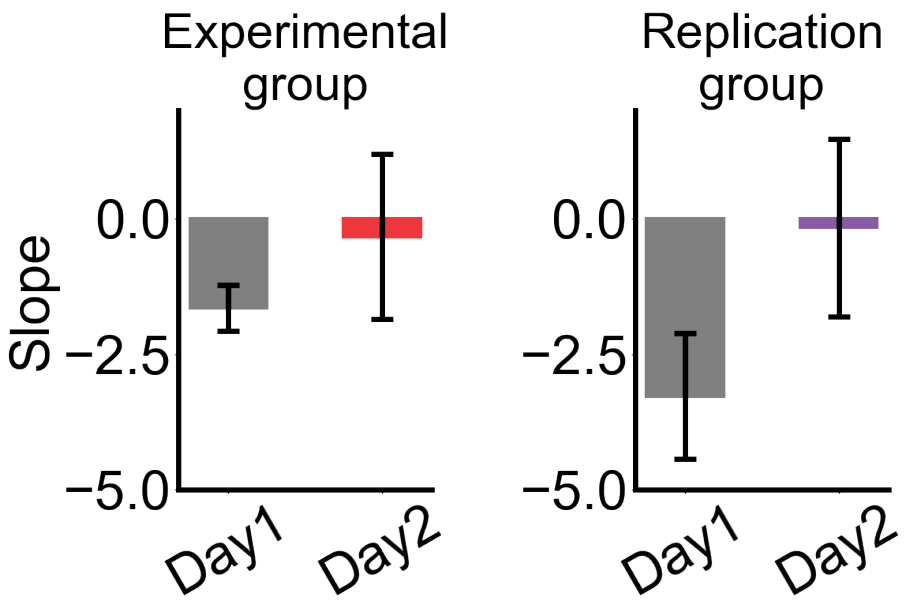

Fig. S1. Learning effect of behavioral performance in Day 1 and Day 2. The error was defined as the distance between the prototype location and the location where participants stopped. On day 1, task errors decreased as a function of experimental sessions, resulting a significantly negative slope for both groups of participants (experimental group: t(9) = -3.90, p = 0.003, two-tailed; Cohen's d = -1.3; replication group: t(9) = -2.82, p = 0.019, Cohen's d = -0.94). No significant learning effect was found on day 2 (experimental group [Red]: t(9) = -0.22, p = 0.834, two-tailed; Cohen's d = -0.07; replication group［Purple］: t(9) = -0.10, p = 0.922, Cohen's d = -0.03). This design eliminates the possibility of a learning effect when examining the spatial periodicity of the HPC. Error bars indicate SEM.

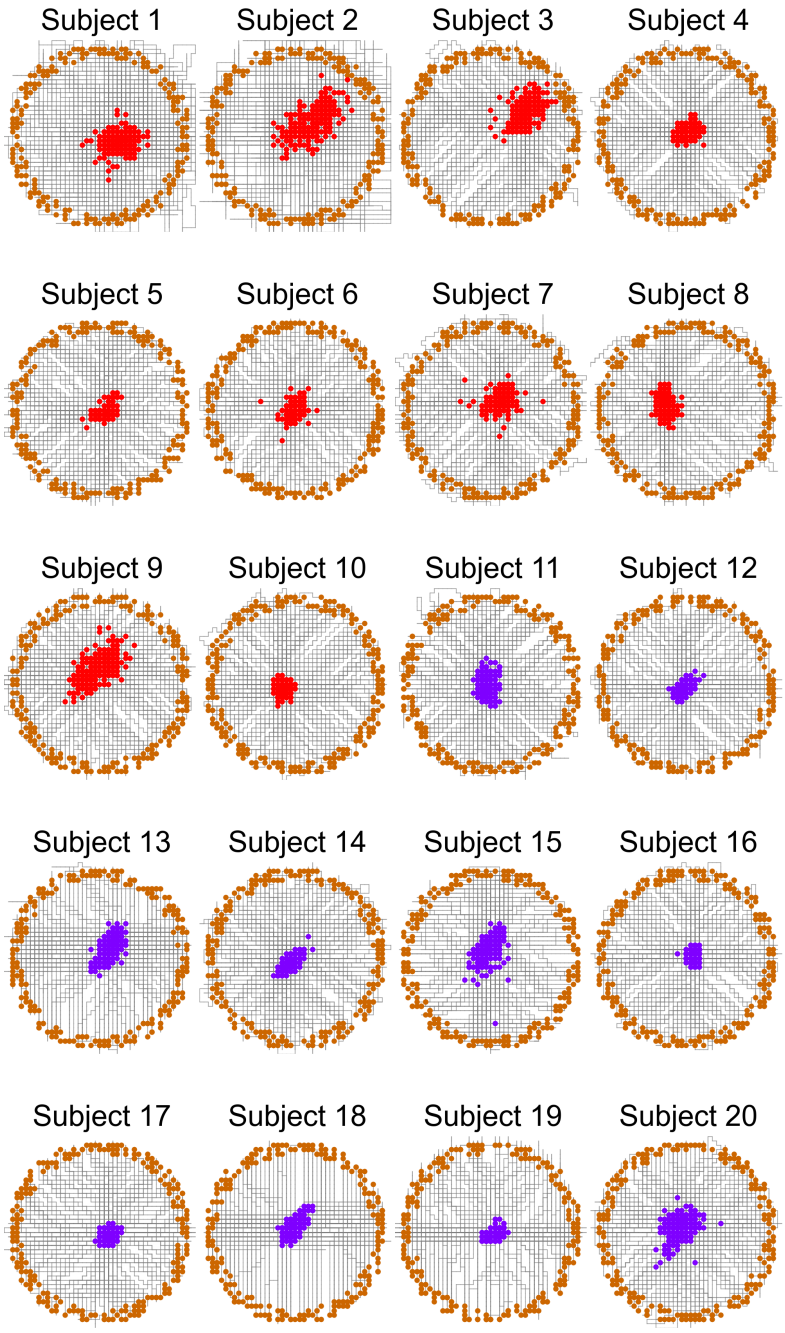

Fig. S2. Movement paths of human participants recorded during MRI scanning. The orange dots represent the starting-locations. The red dots denote the ending locations for the experimental group, while the purple dots represent the ending locations for the replication group. The black lines indicate the movement paths.

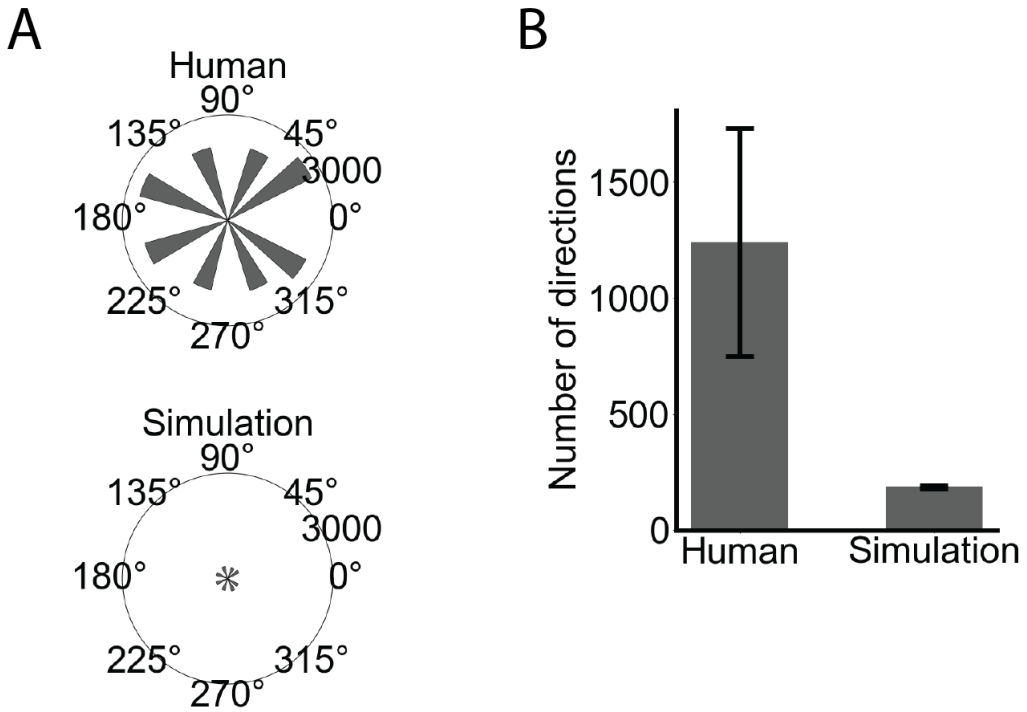

Fig. S3. Number of intercardinal movement directions performed by human participants during the MRI experiment. Intercardinal movement directions were computed for every three consecutive movement steps along a path in each experimental session and for each human participant. A) Cumulative distribution of intercardinal movement directions across 20 participants (top) and controls (bottom). The label "3000" denotes the reference magnitude of the number of directions, consistent for both human participants and controls. B) Human participants exhibited significantly more movement directions compared to controls ($t(19) = 9.353$, $p < 0.001$; two-tailed; Cohen's d = 1.67).

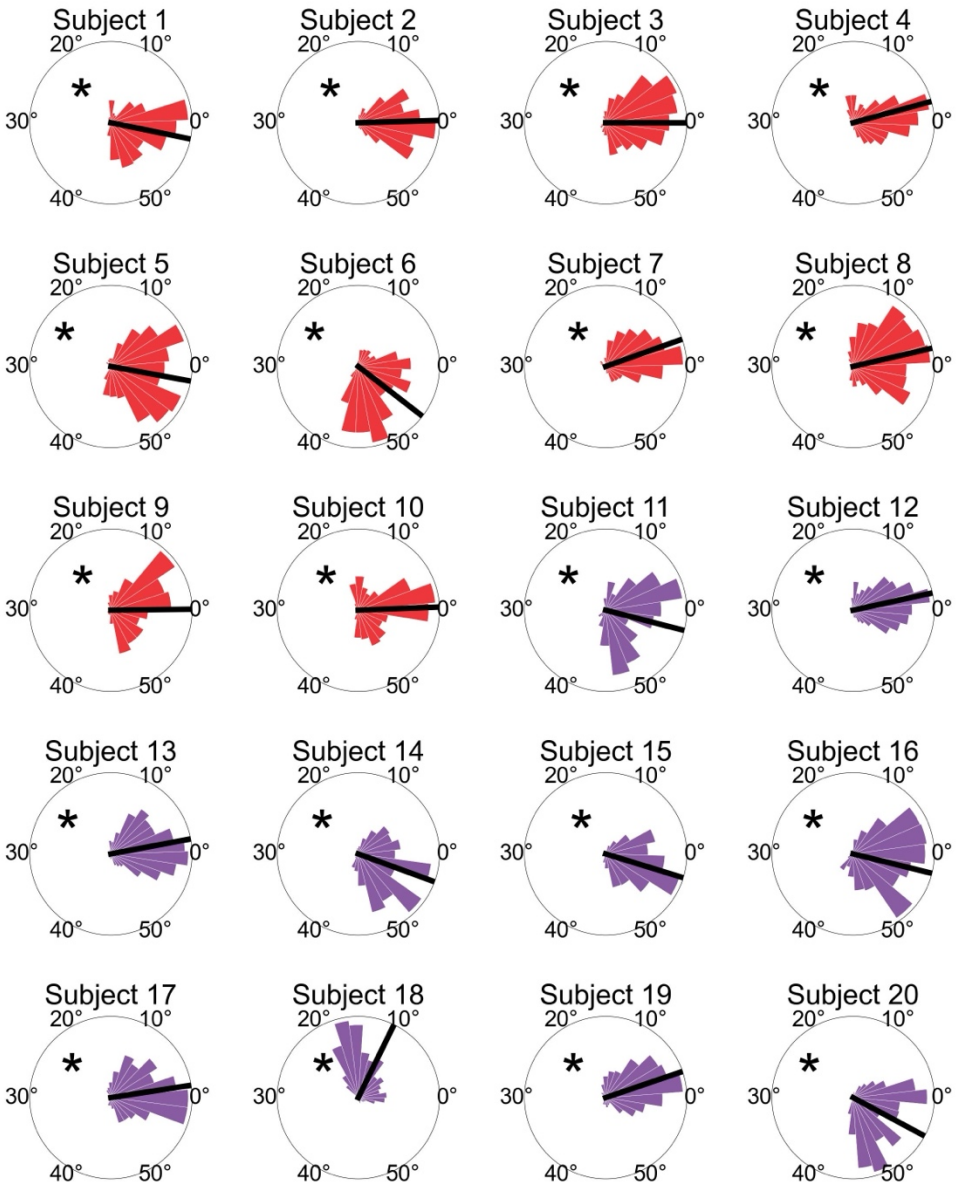

Fig. S4. Distribution of grid orientations in the ERC. The grid orientations ranging from 0° to 60° were computed for each voxel and each participant in both the experimental (red) and replication (purple) group. The uniformity of grid orientations was assessed by Rayleigh test. All participants exhibited significantly clustered grid orientations, indicated by * ($p < 0.05$, Bonferroni corrected). The length of bars represents the number of voxels. The black line denotes the mean of hexagonal orientations.

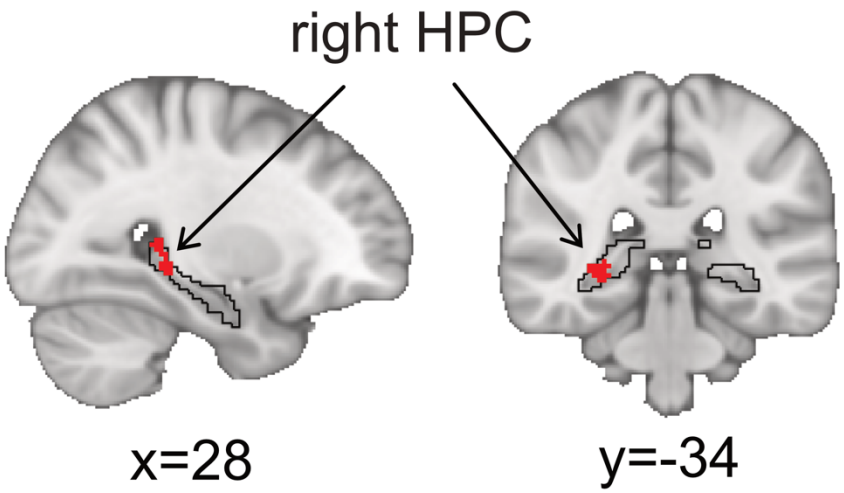

Fig. S5. 3-fold periodicity revealed by sinusoid analysis. Significant cluster was found in the right HPC (initial threshold: $p = 0.05$, two tailed; SVC correction of the bilateral HPC for multiple comparison: $p < 0.05$; Peak MNI coordinate: 30, -33, -4, t(19) = 3.63).

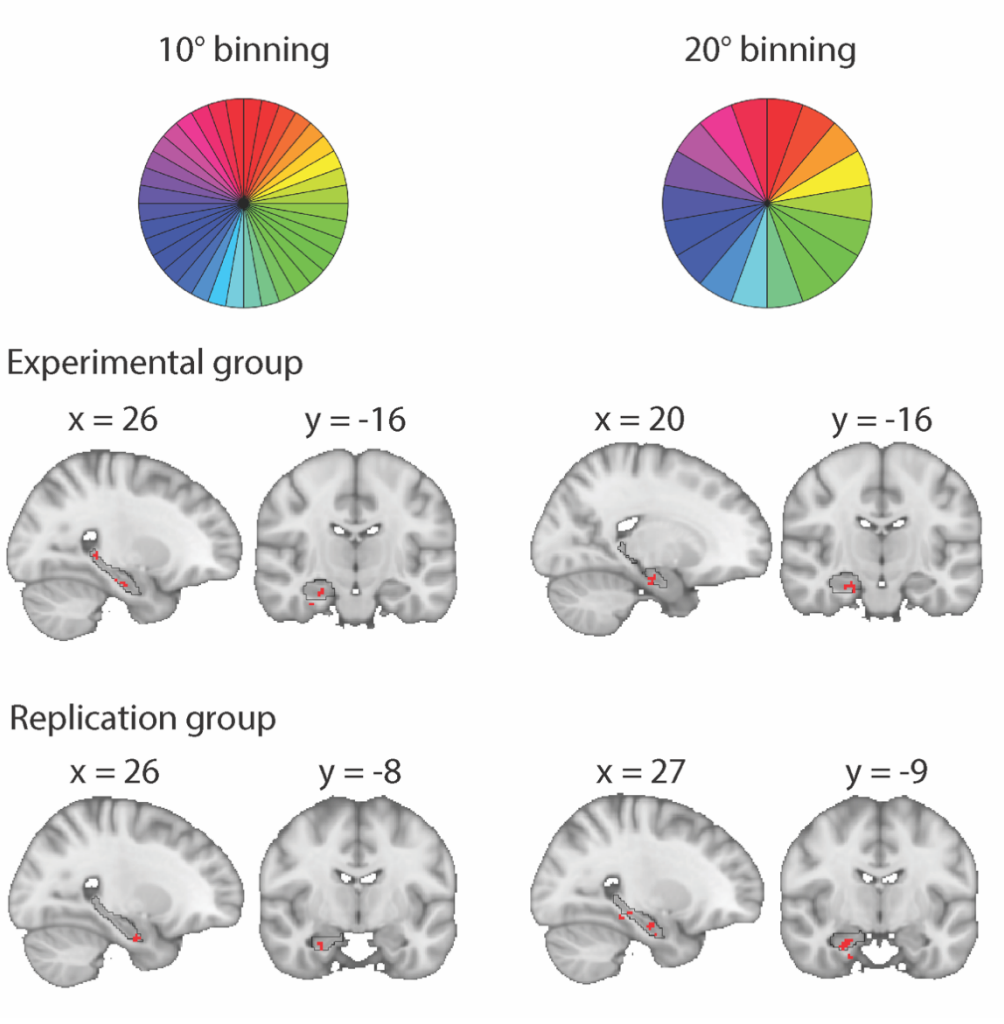

Fig. S6. 3-fold periodicity of the HPC examined using 10° and 20° bin. Significant clusters were consistently revealed in the right HPC (initial threshold: $p = 0.01$, one-tailed; SVC correction of the MTL for multiple comparison: $p < 0.05$; Experimental group & 10° bin: Peak MNI coordinate: 26, -16, -20, t(19) = 5.52; Experimental group & 20° bin: Peak MNI coordinate: 20, -16, -22, t(19) = 3.91; Replication group & 10° bin: Peak MNI coordinate: 26, -8, -24, t(19) = 2.99; Replication group & 20° bin: Peak MNI coordinate: 27, -9, -26, t(19) = 4.06). The x & y value represent the MNI coordinate.

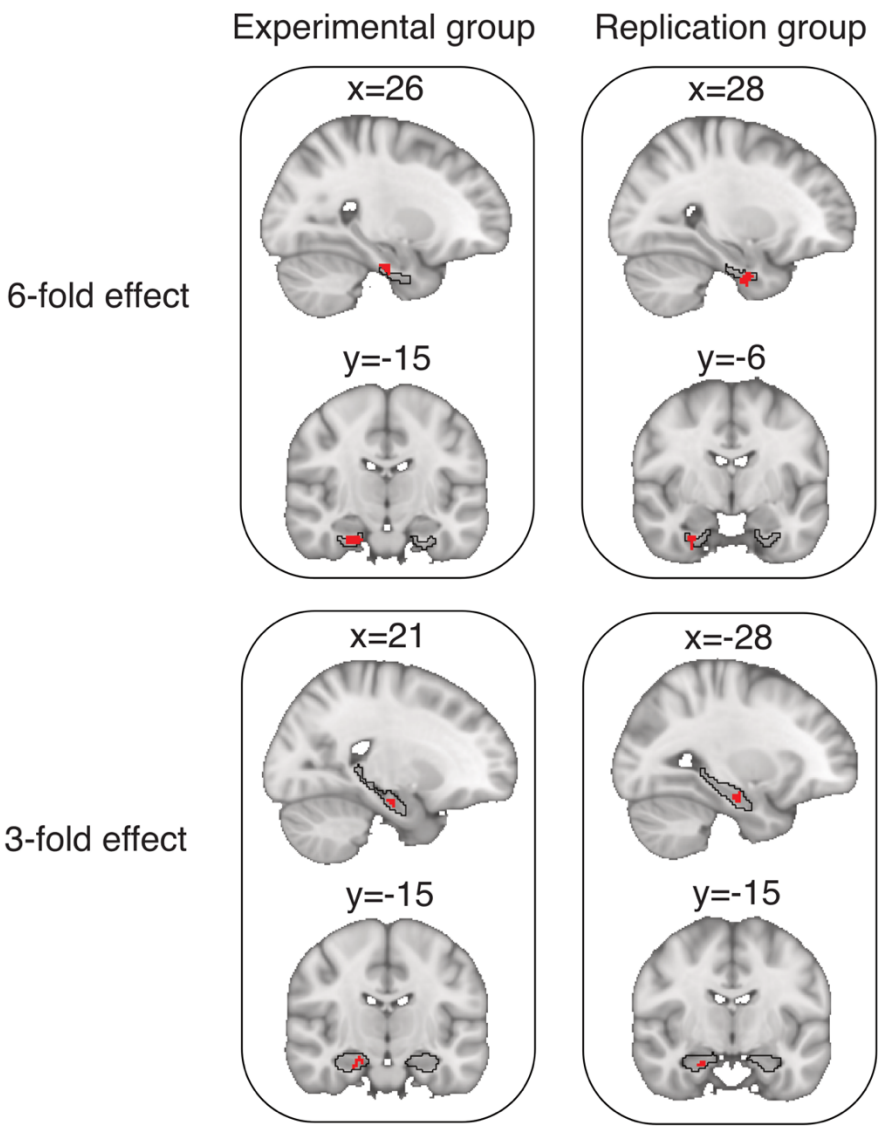

Fig. S7. 6- and 3-fold periodicity revealed in the experimental (10 participants) and replication group (10 participants). These periodic effects were examined using sinusoidal (6-fold) and FFT (3-fold) analysis, respectively. A significant cluster showing 6-fold periodicity was detected in the right ERC (initial threshold: $p = 0.01$, two-tailed. SVC correction of the MTL for multiple comparison: $p < 0.05$; Experimental group: Peak MNI coordinate: 26, -15, -28, t(19) = 4.39; Replication group: Peak MNI coordinate: 27, -10, -38, t(19) = 3.57). 3-fold periodicity revealed a cluster in the right HPC (initial threshold: $p = 0.01$, one-tailed. SVC correction of the MTL for multiple comparison: $p < 0.05$; Experimental group: Peak MNI coordinate: 22, -16, -18, t(19) = 6.60; Replication group: Peak MNI coordinate: 28, -16, -16, t(19) = 7.32).

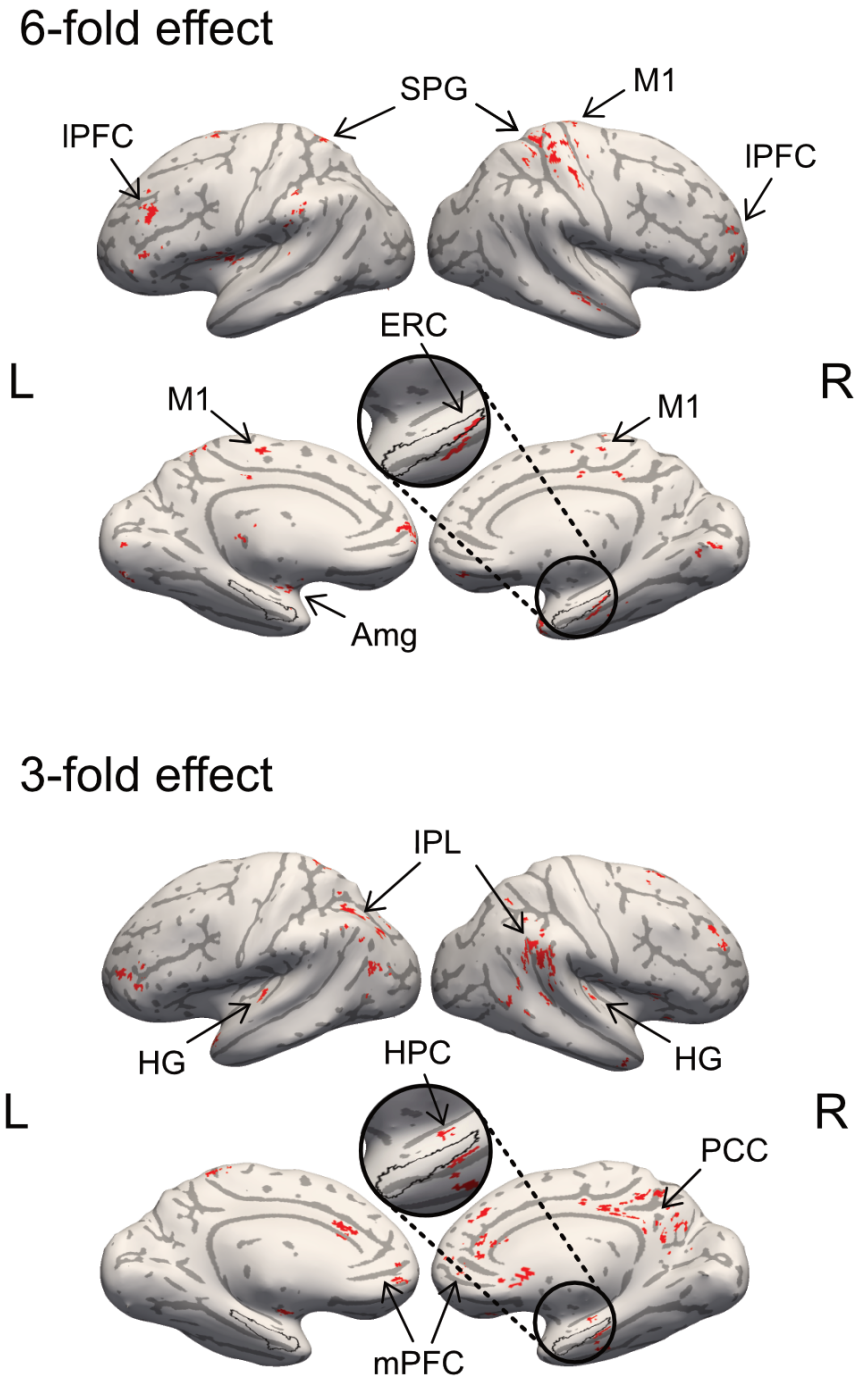

Fig. S8. Whole brain representations of the 6- and 3-fold periodicity (20 participants). Significant clusters (Red) were identified by spectral analysis, which applied an initial threshold of $p = 0.01$ (one-tailed) followed by permutation test for multiple comparison ($p < 0.05$).

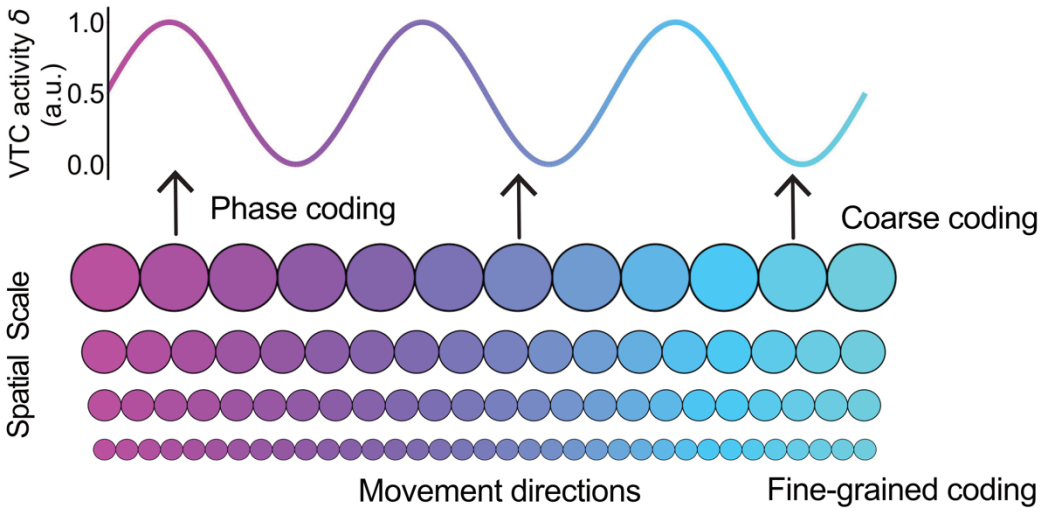

Fig. S9. Phase coding of the HPC activity in spatial domain. The 3-fold periodicity of the HPC may serve as a scaffold to embed future directions towards the goal at each spatial location using multi-scale encoding. In this way, coarse directions are encoded by fewer neurons, while fine-grained directions require a large number of neurons.